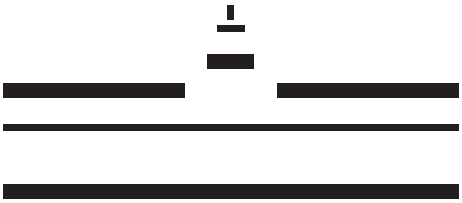

Westfälische
Wilhelms-Universität
Münster

Masterarbeit

Sensitivity of tES Optimization to Different FEM Approaches

Westfälische Wilhelms-Universität Münster
Institut für Numerische und Angewandte Mathematik

eingereicht von:

Nikolas Vogenauer

Gutachter:

Prof. Dr. Carsten Wolters
Institut für Biomagnetismus und Biosignalanalyse, WWU Münster
Prof. Dr. Christian Engwer
Institut für Numerische und Angewandte Mathematik, WWU Münster

Münster, 3.Juli 2019

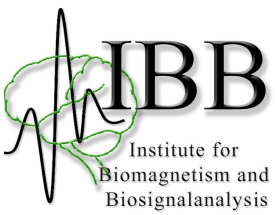

Applied
Mathematics
Münster

Eidesstattliche Erklärung

Hiermit versichere ich, *Nikolas Vogenauer*, dass ich die vorliegende Arbeit selbstständig verfasst und keine anderen als die angegebenen Quellen und Hilfsmittel verwendet habe. Gedanklich, inhaltlich oder wörtlich übernommenes habe ich durch Angabe von Herkunft und Text oder Anmerkung belegt bzw. kenntlich gemacht. Dies gilt in gleicher Weise für Bilder, Tabellen, Zeichnungen und Skizzen, die nicht von mir selbst erstellt wurden.

Münster, 3.Juli 2019

Nikolas Vogenauer

Abstract

Transcranial electric stimulation (tES) is a non-invasive brain stimulation tool. In multi-electrode tES, various optimization approaches are used to investigate how much current should be delivered by each electrode for an optimal targeted and directional modulation of the brain activity. The optimization requires the computation of the tES forward problem, i.e. the simulation of the potential for a bipolar electrode configuration in a volume conductor model. The forward problem has to be solved numerically for a realistic head model, typically by using finite element methods (FEM).

In this thesis, different FEM approaches to solve the forward problem of tES are studied and the influence of these FEM methods on the tES optimization is investigated. Therefore, the continuous Galerkin (CG) and discontinuous Galerkin (DG) FEM are derived and evaluated. Further, an analytical solution for sphere models is introduced. While the accuracy of the FEM solutions is similar in common sphere models, numerical errors can be reduced in models with skull leakages by using DG-FEM.

In the second part, the influence of the CG and DG solutions on various optimization approaches is investigated. The usage of different FEM methods changes significantly the applied current pattern for models with skull leakages.

Contents

List of Figures

1. Introduction

Transcranial electric stimulation (tES) is a non-invasive brain stimulation technique to alter neural excitability by applying weak currents via two or more electrodes placed on the scalp. The emerging portable and easy-to-perform technique involves the delivery of low-intensity currents ($\sim 1 - 2mA$) by a battery-driven stimulator. To alter brain excitability, tES uses either constant, oscillating or randomly alternating currents [43]. tES is increasingly investigated in neuroscientific research and medical therapy for the treatment of neuropsychiatric disorders [11, 35, 43].

The current flow in the brain not only depends on the stimulation intensity and electrode positioning, but is strongly influenced by the individual anatomy of the head tissues [36, 42]. Therefore, the simulation of transcranial volume conduction for anatomically realistic models is important.

The numerical evaluation of the resulting electric potential (or current density field) throughout the head model caused by the injected currents at the electrodes is also called the forward problem of tES. The finite element method (FEM) is the common computational modeling technique for solving the tES forward problem [36, 48, 53]. Thereby, anatomical realistic models of the human head based on magnetic resonance image (MRI) are normally used. In electroencephalography (EEG) and magnetoencephalography (MEG), FEM achieve high numerical accuracy [33, 51], but numerical errors of FEM approaches for tES modeling have not been sufficiently investigated.

In this thesis, the accuracy of the FEM approaches in tES is numerically evaluated. This comparison is performed in simplified approximations of the head by multi-layer sphere models, where the problem can also be solved analytically via spherical series expansions. So far only the continuous Galerkin FEM (CG-FEM) is investigated in tES modeling. In this work, the discontinuous Galerkin FEM (DG-FEM) for tES simulations is also derived, which is presented for EEG in [17]. This approach archives similar accuracy for tES in common sphere models, but DG-FEM is more accurate in models with skull leakages.

The inverse problem of multi-electrode tES is to determine a current injection

pattern that optimally (in a certain sense) stimulates a given target or region of interest. Therby always a trade-off between intensity and focality of the stimulation has to be made [16]. Various optimization approaches are used to generate an optimal solution of the inverse problem [12]. In this thesis, the influence of the CG-FEM and DG-FEM approaches on three different optimization approaches is investigated. We found significant differences between the FEM approaches in the applied current pattern for models with skull leakages.

The implementation of CG-FEM and DG-FEM for solving the tES forward problem is done in *duneuro* [41], a toolbox for forward modeling in neuroscience.

The thesis is structured as follows: The physiological and mathematical background of tES are presented and the forward problem of tES is derived in Chapter 2. In Chapter 3, the FEM approaches to solve the tES forward problem are introduced, the commonly used continuous Galerkin (CG) method and the more recent discontinuous Galerkin (DG) method. Chapter 4 is dedicated to solve the tES forward problem analytically in sphere models using spherical harmonics and to evaluate the convergence of the analytical solution numerically. The FEM approaches are validated in multi-layer sphere models in Chapter 5. We investigate the accuracy of different mesh resolutions and evaluate how skull leakages affect the FEM solutions. Finally, the optimization problem of multi-electrode tES is introduced in Chapter 6. We present different optimization approaches and evaluate them in a sphere model and a realistic head model for both FEM approaches.

2. Basics

In this chapter, we will give the neurological basics and mathematical derivations for the forward problem of transcranial electric stimulation. We start by describing the physiology necessary to understand how electric fields are generated in the human head and how they are influenced by transcranial electric stimulation. Subsequently, the tES forward problem is derived from the quasi-static approximation of Maxwell's equations. To conclude, we will show that this partial differential equation has a unique solution.

2.1. Physiological Background

In the following, the basics of brain activity are explained, to understand how electric fields influence the human brain. The brain is processing and controlling almost all of the human body functions. It communicates through the nervous system via electrochemical signals. The basic elements of the nervous system are nerve cells, called neurons. The human brain contains about 100 billion neurons, which are electrically excitable cells, that process and transmit information [30].
A neuron can be divided into three parts: the dendrites, the cell body called soma and the axon (Figure 2.1). Neurons communicate with each other via synaptic connections. Each neuron has up to $10,000$ of these synapses to other neurons, so they form a large communication network.

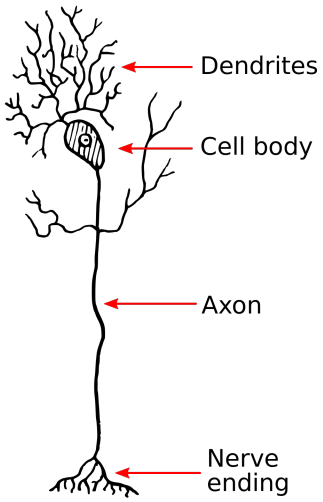

Figure 2.1.: Illustration of a human nerve cell.
Source : *WikimediaCommons*.

Signal transmission works in the following way: At the dendrites, a neuron receives electrical signals from other nerve cells. These signals are transferred to the soma and bundled here. Possibly a new signal will be generated, which

propagates down the axon to other neurons or muscle cells.
Because of the unequal extracellular and intracellular distribution of positive and negative ions, an inactive neuron has a resting potential of approximately -70 mV [26].
The signal transmission is based on alterations in the resting potential of the membranes of the presynaptic and postsynaptic neurons. If a signal reaches the axon of the presynaptic neuron, neurotransmitter will be released here. The neurotransmitter will diffuse through the synaptic cleft and be received from the membrane at the dendrite of the postsynaptic neuron. In the dendrite, the neurotransmitter will cause a potential change, called the postsynaptic potential. This can have an excitatory or an inhibitory effect on the postsynaptic neuron.
All signals from the dendrites are summed up in the soma. When the depolarization is bigger than a certain threshold in the postsynaptic cell, this neuron fires, so a new action potential is generated and moves down the axon (also see Figure 2.2).

2.2. Transcranial Electric Stimulation

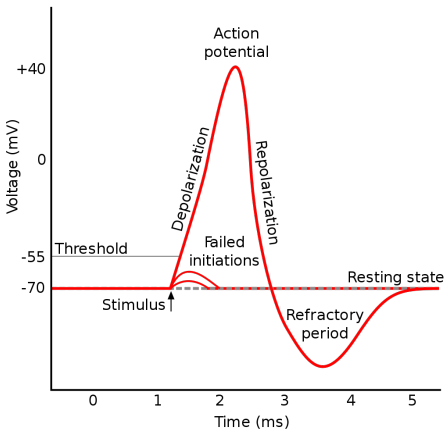

Figure 2.2.: The shape of an action potential.
Source : *WikimediaCommons*.

In this section, we shortly explain how transcranial electric stimulation (tES) affects the neuronal brain functions. tES are non-invasive brain stimulation techniques, where weak electrical currents are applied to the brain by surface electrodes. The four main methods of low-intensity tES are transcranial direct current stimulation (tDCS), transcranial alternating current stimulation (tACS), transcranial pulsed current stimulation (tPCS) and transcranial random noise stimulation (tRNS) [43]. The electric field induced by tES is in contrast to transcranial magnetic stimulation (tMS) subthreshold, so it is not strong enough to trigger an action potential in a nerve cell [5, 35]. The best known and most used method is tDCS.
During tDCS, the electric field will change the resting membrane potential and

therefore can influence the synaptic signal transmission between neurons and change the firing rate of each nerve cell (Figure 2.2). Depending on the stimulation paradigm, tDCS can increase or decrease neuronal excitability [37, 38]. However, it is more likely that the current has a higher effect normal to the cortical surface than tangential [45]. tDCS can alter synaptic plasticity, the ability of synapses to strengthen or weaken over time [32]. The duration of the after-effect of tDCS depends on the stimulation polarity, time and intensity [43].
In studies tDCS has been used to treat Parkinson's disease [7], Alzheimer [21], stroke [31] and depression [39].

2.3. Maxwell's Equations

To model the electromagnetic effects in the human brain, the Maxwell's equations are used [10, 27]. The Maxwell's equations are a system of partial differential equations, which describe the interactions between electric and magnetic fields. We note that the permeability of tissues in the head is that of free space, i.e. μ=μ_0.

Definition 2.1 (Maxwell's equations of electromagnetism)
The Maxwell's equations can be formulated as

$$\nabla \cdot \mathbf{E} = \frac{\rho}{\epsilon_0} \tag{2.1}$$

$$\nabla \cdot \mathbf{B} = 0 \tag{2.2}$$

$$\nabla \times \mathbf{E} = -\frac{\partial B}{\partial t} \tag{2.3}$$

$$\nabla \times \mathbf{B} = \mu \left(J + \epsilon_0 \frac{\partial E}{\partial t} \right), \tag{2.4}$$

where $\mathbf{E}$ denotes the electric field, $\mathbf{B}$ the magnetic field, ρ the charge density, J the current density, ϵ_0 the electrical permittivity and μ the magnetic permeability.
In the considered low-frequency band (below 1000 Hz), the electric field $\mathbf{E}$ and magnetic field $\mathbf{B}$ can be described by the quasi-static approximation of the Maxwell's equations and the time derivatives can be neglected [27, 44]. In the

quasi-static approximation, we get from (2.3)

$$\nabla \times \mathbf{E} = 0 \tag{2.5}$$

and hence, the electric field can be expressed by

$$\mathbf{E} = -\nabla u \tag{2.6}$$

for a scalar potential u.

2.4. The tES Forward Problem

We will now derive the forward problem of tES [34]. Note that the forward problem of tES is the same as the forward problem in electrical impedance tomography (EIT).
The current density J can be divided into source currents J^s and conduction currents J^c. In the conductive medium, we can apply Ohm's law $J^c = -\sigma\nabla u$ and get

$$J = J^s + J^c = J^s + \sigma\mathbf{E} = J^s - \sigma\nabla u, \tag{2.7}$$

where $\sigma : \Omega \to \mathbb{R}^{3\times 3}$ denotes the conductivity tensor.
In tES, the source term J^s is typically considered zero:

$$J = -\sigma\nabla u. \tag{2.8}$$

Taking the divergence of equation (2.4) under the quasi-static assumption, using the fact that $\nabla \cdot (\nabla \times \mathbf{B}) = 0$ and applying (2.8) gives

$$\nabla \cdot (\sigma\nabla u) = 0 \qquad \text{in } \Omega. \tag{2.9}$$

Because current is applied at surface electrodes and the head is an electric isolator, we get inhomogeneous Neumann boundary conditions on the head surface $\partial\Omega$

$$\langle \sigma\nabla u, n\rangle = I \qquad \text{on } \partial\Omega, \tag{2.10}$$

where n is the surface normal and I is the applied current pattern at the electrodes.
Then the tES forward problem reads as follows:

Definition 2.2 (tES forward problem)
The tES forward problem consists in finding a solution u of the following Poisson equation with inhomogeneous Neumann boundary conditions:

$$\nabla \cdot \sigma \nabla u = 0 \quad \text{in } \Omega \tag{2.11}$$
$$\langle \sigma \nabla u, n \rangle = I \quad \text{on } \partial\Omega\,, \tag{2.12}$$

which has to fulfill the necessary condition $\int_{\partial\Omega} I \,\mathrm{d}s = 0$, because

$$\int_{\partial\Omega} I \,\mathrm{d}s = \int_{\partial\Omega} \langle \sigma \nabla u, n \rangle \,\mathrm{d}s = \int_{\Omega} \nabla \cdot \sigma \nabla u \,\mathrm{d}x = \int_{\Omega} 0 \,\mathrm{d}x = 0. \tag{2.13}$$

The solution of the tES forward problem is the potential field u in the volume conductor Ω, from which we can then also calculate the electric field or current density field.
The tES forward problem only has a classical solution, i.e. $u \in C^2(\Omega) \cap C^0(\bar{\Omega})$, for continuous conductivities $\sigma \in C^1(\Omega)$ [25]. Usually, the conductivity is discontinuous at tissue interfaces, i.e. $\sigma \in L^\infty(\Omega)$. Therefore, we will search for a weak solution of the TES forward problem. Existence and uniqueness of the weak solution will be shown in the next section.

2.5. Existence and Uniqueness

We will start with the tES forward problem in the strong formulation from Definition 2.2. Then the weak formulation of the tES forward problem is derived. Finally, we will show that there exists a solution of the weak formulation and that it is unique.
In order to derive a weak formulation for the tES forward model, we multiply (2.11) with a test function $v \in C_0^\infty$ and apply integration by parts to obtain

$$\begin{aligned} 0 &= \int_{\Omega} (\nabla \cdot \sigma \nabla u) v \,\mathrm{d}x \\ &= -\int_{\Omega} \langle \sigma \nabla u, \nabla v \rangle \,\mathrm{d}x + \int_{\partial\Omega} \langle \sigma \nabla u, n \rangle v \,\mathrm{d}s. \end{aligned} \tag{2.14}$$

Using the inhomogeneous Neumann boundary conditions (2.12) yields

$$\int_{\Omega} \langle \sigma \nabla u, \nabla v \rangle \,\mathrm{d}x = \int_{\partial\Omega} I v \,\mathrm{d}s. \tag{2.15}$$

The weak formulation is then as follows:

Definition 2.3 (Weak Formulation)
Find $u \in V$ such that

$$a(u, v) = l(v) \tag{2.16}$$

holds for all test functions $v \in V$, with

$$a(u, v) = \int_\Omega \langle \sigma \nabla u, \nabla v \rangle \, \mathrm{d}x \tag{2.17}$$

$$l(v) = \int_{\partial\Omega} Iv \, \mathrm{d}s. \tag{2.18}$$

To show existence and uniqueness of a solution to the weak formulation, we want to use the Lemma of Lax-Milgram (Theorem A.1). Therefore, we have to find a feasible function space V for the weak formulation. A natural choice is the Sobolev space $H^1(\Omega)$ because it is a set of L^2 functions, whose weak derivatives are again L^2 functions (for mathematical details see Appendix A.1). The solution with pure Neumann boundary conditions (2.12) is only unique up to a constant. To ensure the uniqueness of the solution, there are several approaches valid. We will use the condition, that the potential has zero mean:

$$\int_\Omega u \, \mathrm{d}x = 0. \tag{2.19}$$

We will include this condition by restricting our Sobolev space to

$$H^1_*(\Omega) := \{v \in H^1(\Omega) : \int_\Omega v \, \mathrm{d}x = 0\}, \tag{2.20}$$

the Sobolev space with zero mean. To ensure that $l(\cdot)$ is a continuous functional in $(H^1(\Omega))'$ the applied current I has to be in the space

$$H^{-1/2}_*(\partial\Omega) = \{v \in H^{-1/2}(\partial\Omega) \mid \int_{\partial\Omega} v \, \mathrm{d}s = 0\} \tag{2.21}$$

with $H^{-1/2}(\partial\Omega)$ being the dual space of $H^{1/2}(\partial\Omega)$, which is the standard Sobolev space for Neumann boundary values on $\partial\Omega$, which fulfills the necessary condition (2.13).
We will now show that there is a solution to the weak formulation of the tES forward problem:
Find $u \in V := H^1(\Omega)$ such that

$$a(u, v) := \langle \sigma \nabla u, \nabla v \rangle_{L^2(\Omega)} = \langle I, v \rangle_{H^{-1/2}(\Omega) \times H^{1/2}(\Omega)} =: l(v). \tag{2.22}$$

Lemma 2.1 *The bilinearform $a(\cdot,\cdot)$ is bounded on $H^1(\Omega) \times H^1(\Omega)$.*

Proof. Let σ_{max} be the largest eigenvalue of $\sigma(x)$. Then holds

$$\begin{aligned} |a(u,v)| &= |\int_\Omega \langle \sigma \nabla u, \nabla v \rangle \, \mathrm{d}x| \\ &\leq \sigma_{max} \int_\Omega \|\nabla u\| \|\nabla v\| \, \mathrm{d}x \\ &\leq \sigma_{max} \|\nabla u\|_{L^2(\Omega)} \|\nabla v\|_{L^2(\Omega)} \\ &\leq \sigma_{max} \|u\|_{H^1(\Omega)} \|v\|_{H^1(\Omega)}. \end{aligned}$$

□

Lemma 2.2 *The bilinearform $a(\cdot,\cdot)$ is $H^1_*(\Omega)$-elliptic.*

Proof. [55] □

Lemma 2.3 *The functional $l(\cdot)$ is well-defined and bounded in $H^1(\Omega)$.*

Proof. For $v \in H^1(\Omega)$, the Trace Theorem A.2 can be applied and therefore can be concluded that

$$\begin{aligned} |l(v)| &= \int_{\partial\Omega} |Iv| \, \mathrm{d}s \\ &\leq \|I\|_{H^{-1/2}(\partial\Omega)} \|v\|_{H^{1/2}(\partial\Omega)} \\ &\leq C \|I\|_{H^{-1/2}(\partial\Omega)} \|v\|_{H^1(\Omega)}. \end{aligned}$$

□

Theorem 2.4 *(Existence and Uniqueness)*
Let $\Omega \subset \mathbb{R}^3$ be an open bounded domain with a smooth boundary. Then the weak formulation has a unique solution $u \in H^1_*(\Omega)$.

Proof. The bilinearform $a(\cdot,\cdot)$ is bounded (Lemma 2.1) and $H^1_*(\Omega)$-elliptic (Lemma 2.2), the functional $l(\cdot)$ is bounded (Lemma 2.3). Thus, the Lemma of Lax-Milgram (Lemma A.1) can be applied, so there is exactly one $u \in H^1_*(\Omega)$ that solves the weak formulation. □

3. FEM Approaches

In this chapter, we will deal with the numerical calculation of the weak solution. We will use the finite element method (FEM), which is a commonly used technique in tES [36, 48, 53]. We will introduce the continuous Galerkin (CG) and the discontinuous Galerkin (DG) finite element methods.

3.1. The Continuous Galerkin Finite Element Method

In this section, we will give the theory of the continuous finite element method [8, 9] for solving the tES forward problem. To apply the CG approach, we will use the Galerkin method for the discretization of the infinite space V. The domain Ω is then divided into easier geometries, normally tetrahedrons or hexahedrons. Finally, we will take a closer look at the Lagrangian finite element space V_h.

Galerkin Method

The basic idea of the finite element method is to find discrete approximations to the solution of the weak formulation

$$\text{Find } u \in V : a(u, v) = l(v) \text{ for all } v \in V. \tag{3.1}$$

In this thesis, we will for discretization use the Galerkin method. We replace the infinite-dimensional space V by a finite-dimensional space V_h, where h denotes a discretization parameter. We then get the discrete weak formulation

$$\text{Find } a(u_h, v_h) = l(v_h) \text{ for all } v_h \in V_h \tag{3.2}$$

with

$$a(u_h, v_h) = \int_\Omega \langle \sigma \nabla u_h, \nabla v_h \rangle \, \mathrm{d}x \tag{3.3}$$

$$l(v_h) = \int_{\partial\Omega} I v_h \, \mathrm{d}s. \tag{3.4}$$

u_h is called the discrete solution of the weak formulation (3.1). An error estimate of the finite-element approximation is given by Céa's Lemma.

Theorem 3.1 *(Céa's Lemma)*
Let $(V, \langle \cdot, \cdot \rangle)$ be a Hilbert space, $a(\cdot, \cdot)$ a continuous, coercive bilinearform and $l \in V'$ a continuous, linear functional. If $u \in V$ solves the weak formulation (3.1), then the discrete solution $u_h \in V_h$ of the discrete weak formulation (3.2) is obtained with

$$\|u - u_h\|_V \leq \frac{C}{c} \inf_{v_h \in V_h} \|u - v_h\|_V \tag{3.5}$$

where C is the continuity constant and c is the coercivity constant of $a(\cdot, \cdot)$.

Proof. [8] □

Céa's Lemma shows that the discretization error is proportional to the approximation error and that the accuracy of the numerical solution strongly depends on the choice of the subspace V_h.
We will later deal with the concrete choice of the subspace V_h for the CG approach. For now we will assume it is given and want to consider the calculation of the Galerkin approximation.
Let $N := \dim(V_h)$ and $\{\psi_1, \ldots, \psi_N\}$ be the basis of the finite element space V_h. We can then write our discrete solution $u_h \in V_h$ as:

$$u_h = \sum_{j=1}^{N} u_j \psi_j, \tag{3.6}$$

and insert it into the discrete weak formulation (3.2), to get

$$a(\sum_{j=1}^{N} u_j \psi_j, \psi_i) = \sum_{j=1}^{N} u_j a(\psi_j, \psi_i) = l(\psi_i). \tag{3.7}$$

So overall this leads to the linear equation system

$$\boldsymbol{K}\boldsymbol{u} = \boldsymbol{b}, \tag{3.8}$$

where the stiffness matrix $\boldsymbol{K} \in \mathbb{R}^{N \times N}$, the load vector $\boldsymbol{b} \in \mathbb{R}^N$ and the solution vector $\boldsymbol{u} \in \mathbb{R}^N$ are defined by

$$\boldsymbol{K} = (a(\psi_i, \psi_j))_{1 \leq i,j \leq N} \tag{3.9}$$

$$\boldsymbol{b} = l(\psi_i)_{1 \leq i \leq N} \tag{3.10}$$

$$\boldsymbol{u} = (u_j)_{1 \leq j \leq N}. \tag{3.11}$$

The discrete solution u_h is then obtained by solving this linear equation system. Therefore, a numerical solver like the algebraic multigrid conjugate gradient (AMG-CG) method can be used.

The continuous finite element methods is a special Galerkin approximation for a certain class of subspaces $V_h \subset V$:

- The domain is triangulated into $\mathcal{T}_h$, i.e. divided into non-overlapping polyhedral elements T.
- The functions $v_h \in V_h$ are piecewise polynomials, i.e. the restriction of $v_h \in V_h$ onto an element $T \in \mathcal{T}_h$ is polynomial.
- The basis $\{\phi_i\}$ of V_h has local support, i.e. the basis functions ϕ_i are only on a few elements non-zero.

We will now take a look at the triangulation of the domain Ω.

Triangulation

Definition 3.1 (Triangulation)
A triangulation of a domain $\Omega \subset \mathbb{R}^d$ is a set $\mathcal{T}_h = \{T_1, \ldots, T_M\}$ of open sets $T_i \subset \Omega$ such that:

$$\bigcup_{i=1}^{M} \bar{T}_i = \bar{\Omega} \tag{3.12}$$

$$T_i \cap T_j = \emptyset \qquad \text{for } i \neq j \tag{3.13}$$

$$h := \max\{diam(T) \,|\, T \in \mathcal{T}_h\} \tag{3.14}$$

Definition 3.2 (Admissible Triangulation)
A triangulation $\mathcal{T}_h$ is called admissible if every non-empty intersection $\bar{T}_i \cap \bar{T}_j$, $i \neq j$ is either a common vertex, a common edge or in three dimensions a common face shared by T_i and T_j.

Definition 3.3 (Shape-Regular Family of Triangulations)
A family of triangulations $\{\mathcal{T}_h\}$ is called shape-regular if there is a number $\kappa > 0$ such that every T in $\mathcal{T}_h$ contains a circle of radius ρ_T with

$$\rho_T \geq h_T/\kappa, \tag{3.15}$$

where h_T denotes the diameter of T.

Definition 3.4 (Uniform Family of Triangulations)
A family of triangulations $\{\mathcal{T}_h\}$ is called uniform if there is a number $\kappa > 0$ such that every T in $\mathcal{T}_h$ contains a circle of radius ρ_T with

$$\rho_T \geq h/\kappa. \tag{3.16}$$

The finite element space V_h for the continuous Galerkin method is defined based on the triangulation $\mathcal{T}_h(\Omega)$.

Finite Element Space

Definition 3.5 (Finite Element Space)
The finite element space V_h is defined as the space of continuous, piecewise polynomial functions of order k

$$V_h := \{v_h \in C^0(\Omega) : v_{h|T} \in P^k(T) \text{ for all } T \in \mathcal{T}_h(\Omega)\}, \tag{3.17}$$

where $P^k(T)$ denotes the polynomial space on T.

The choice of the polynomial space P^k depends on the choice of triangulation elements. For tetrahedrons, we will use the space

$$P_k(T) := \text{span}\left\{\prod_{i=1}^{d} x_i^{\alpha_i} : x \in T, \alpha \in \mathbb{N}^d, \sum_{i=1}^{d} \alpha_i \leq k\right\}. \tag{3.18}$$

For hexahedrons, we will choose

$$Q_k(T) := \text{span}\left\{\prod_{i=1}^{d} x_i^{\alpha_i} : x \in T, \alpha \in \mathbb{N}^d, \max_i \alpha_i \leq k\right\}. \tag{3.19}$$

Definition 3.6 (Lagrangian Basis Function)
Let $x_1, \ldots, x_N$ be the vertices of the triangulation $\mathcal{T}_h(\Omega)$ and the basis consists of linear basis functions $\phi_i, i = 1, \ldots, N$. Then the basis functions are called

Lagrangian basis functions or hat functions if

$$\phi_i(x_j) = \begin{cases} 1 \text{ for } i = j \\ 0 \text{ for } i \neq j \end{cases} \tag{3.20}$$

holds.

So in the case of a Lagrangian basis, every function ϕ_i has only support on the adjacent elements to the vertex x_i. That implies that the stiffness matrix $\boldsymbol{K}$ is sparse.

3.2. The Discontinuous Galerkin Finite Element Method

In this section, we introduce the discontinuous Galerkin (DG) method for the numerical solution of the tES forward problem. Other than in CG-FEM, in DG-FEM the potential is only locally continuous over each element, but not globally, because the finite element space is non-conforming $V_h \not\subset V$.
This section mainly follows [1, 15, 17].
Like in the CG-FEM (Section 3.1), let $\mathcal{T}_h(\Omega)$ be a conforming triangulation of the domain. In the DG-FEM, we also need to define the internal and external skeleton of the triangulation.

Definition 3.7 (Skeleton) For a triangulation $\mathcal{T}_h(\Omega)$ the internal skeleton is denoted by

$$\Gamma_{int} := \{\gamma_{e,f} = \partial T_e \cap \partial T_f | T_e, T_f \in T_h(\Omega), T_e \neq T_f, |\gamma_{e,f}| > 0\} \tag{3.21}$$

and the external skeleton by

$$\Gamma_{ext} := \{\gamma_e = \partial T_e \cap \partial\Omega | T_e \in T_h(\Omega), |\gamma_e| > 0\}. \tag{3.22}$$

Then, the corresponding skeleton is defined by

$$\Gamma = \Gamma_{int} \cup \Gamma_{ext}. \tag{3.23}$$

As discontinuous finite element space, we chose the broken polynomial space.

Definition 3.8 (Broken Polynomial Spaces) On a triangulation $\mathcal{T}_h$ the broken polynomial spaces of degree k are defined as

$$V_h := \{v \in L^2(\Omega) | v_{|T} \in \mathcal{P}^k \text{ for all } T \in \mathcal{T}_h(\Omega)\} \tag{3.24}$$

with $\mathcal{P}^k$ being the space of local polynomials of degree k.

These functions do not have any continuity constraint between elements, but are elementwise polynomials. The choice of the polynomial space P^k depends on the choice of triangulation elements. For tetrahedrons, the space $P_k(T)$ and for hexahedrons $Q_k(T)$ will be used as in Section 3.1. Because functions in V_h may be discontinuous across element interfaces, the jump and the average of a function u over an interface are define.

Definition 3.9 (Jump) The jump of a piecewise continuous function u between two adjoint elements $T_e, T_f \in \mathcal{T}_h(\Omega)$ is defined as

$$[\![u]\!]_{e,f} := u_{|T_e} \cdot n_{T_e} + u_{|T_f} \cdot n_{T_f} \tag{3.25}$$

Definition 3.10 (Average) The average of a piecewise continuous function u on the interface $\gamma_{e,f}$ between two adjoint elements $T_e, T_f \in \mathcal{T}_h(\Omega)$ is defined as

$$\{u\}_{e,f} := w_e u_{|T_e} + w_f u_{|T_f} \tag{3.26}$$

with weights w_e and w_f, which are defined by [18]:

$$w_e := \frac{\sigma_f}{\sigma_f + \sigma_e} \text{ and } w_f := \frac{\sigma_e}{\sigma_f + \sigma_e}. \tag{3.27}$$

Then the following property holds [15]:

$$[\![uv]\!]_{e,f} = [\![u]\!]_{e,f}\{v\}_{e,f} + \{u\}_{e,f}[\![v]\!]_{e,f}. \tag{3.28}$$

Galerkin Method

Also in the discontinuous FEM, we look at the weak formulation in Definition 2.3 of the tES forward problem

$$\text{Find } u \in V : a(u, v) = l(v) \text{ for all } v \in V. \tag{3.29}$$

We again use the Galerkin method to obtain a solution $u_h \in V_h$ of the forward problem, but this time our finite element space is non-conforming, i.e. $V_h \not\subset V$.

Because of that, we do not get the discrete weak formulation directly from the weak formulation. Instead, the discontinuities across the element boundaries will cause additional consistency terms on the internal skeleton Γ_{int}. Therefore, we multiply with a test function $v_h \in V_h$ and integrate over the domain Ω

$$\int_\Omega (\nabla \cdot \sigma \nabla u_h) v_h \, \mathrm{d}x = 0. \tag{3.30}$$

We use the triangulation $\mathcal{T}_h(\Omega)$ to decompose the integral

$$\int_\Omega (\nabla \cdot \sigma \nabla u_h) v_h \, \mathrm{d}x = \sum_{T_e \in \mathcal{T}_h} \int_{T_e} (\nabla \cdot \sigma \nabla u_h) v_h \, \mathrm{d}x. \tag{3.31}$$

Because $v_h \in V_h$ is not globally continuous, we apply integration by parts on each element $T_e \in \mathcal{T}_h(\Omega)$:

$$= - \sum_{T_e \in \mathcal{T}_h} \int_{T_e} \langle \sigma \nabla u_h, \nabla v_h \rangle \, \mathrm{d}x + \sum_{T_e \in \mathcal{T}_h} \int_{\partial T_e} \langle \sigma \nabla u_h, n \rangle v_h \, \mathrm{d}s \tag{3.32}$$

The second term can be divided into external and internal skeleton

$$\begin{aligned} = - \int_\Omega \langle \sigma \nabla u_h, \nabla v_h \rangle \, \mathrm{d}x + \int_{\partial\Omega} \underbrace{\langle \sigma \nabla u_h, n \rangle}_{=I} v_h \, \mathrm{d}s \\ + \int_{\Gamma_{int}} [\![(\sigma \nabla u_h) v_h]\!] \, \mathrm{d}s \end{aligned} . \tag{3.33}$$

Using the property (3.28) and hence

$$\begin{aligned} = - \int_\Omega \langle \sigma \nabla u_h, \nabla v_h \rangle \, \mathrm{d}x + \int_{\partial\Omega} I v_h \, \mathrm{d}s \\ + \int_{\Gamma_{int}} \underbrace{[\![\sigma \nabla u_h]\!]}_{=0} \{v_h\} + \{\sigma \nabla u_h\} [\![v_h]\!] \, \mathrm{d}s. \end{aligned} \tag{3.34}$$

At each interface the normal component of the current density $(\sigma \nabla u_h \cdot n_\gamma)$ is continuous, so for the jump we get $[\![\sigma \nabla u_h]\!]_{e,f} = 0$.
Then the discrete weak formulation becomes:

$$\text{Find } u_h \in V_h : a(u_h, v_h) = l(v_h) \text{ for all } v_h \in V_h \tag{3.35}$$

with

$$a(u_h, v_h) = \int_\Omega \langle \sigma \nabla u_h, \nabla v_h \rangle \, \mathrm{d}x - \int_{\Gamma_{int}} \{\sigma \nabla u_h\} [\![v_h]\!] \, \mathrm{d}s \tag{3.36}$$

$$l(v_h) = \int_{\partial\Omega} I v_h \, \mathrm{d}s. \tag{3.37}$$

We add a symmetry term to guarantee adjoint consistency

$$a^{symm}(u_h, v_h) = -\int_{\Gamma_{int}} \{\sigma \nabla v_h\} [\![u_h]\!] \, \mathrm{d}s. \tag{3.38}$$

Then we extend the left-hand side by a penalty term to ensure coercivity

$$J(u_h, v_h) = \eta \int_{\Gamma_{int}} \frac{\hat{\sigma}_\gamma}{h_\gamma} [\![u_h]\!] [\![v_h]\!] \, \mathrm{d}s \tag{3.39}$$

with the penalty parameter η and $\hat{\sigma}_\gamma$ being the harmonic averages of the conductivities of the adjacent elements [14]

$$\hat{\sigma}_{\gamma_{e,f}} := \frac{2\sigma_e \sigma_f}{\sigma_e + \sigma_f} \tag{3.40}$$

and h_γ being a local mesh width parameter [22]

$$h_{\gamma_{e,f}} := \frac{\min(|T_e|, |T_f|)}{|\gamma_{e,f}|}. \tag{3.41}$$

This yields the symmetric weighted interior penalty discontinuous Galerkin method (SWIPG):
Find $u_h \in V_h$ such that

$$a(u_h, v_h) + J(u_h, v_h) = l(v_h) \text{ for all } v_h \in V_h, \tag{3.42}$$

where

$$\begin{aligned} a(u_h, v_h) = &\int_\Omega \langle \sigma \nabla u_h, \nabla v_h \rangle \, \mathrm{d}x \\ &- \int_{\Gamma_{int}} \{\sigma \nabla u_h\} [\![v_h]\!] + \{\sigma \nabla v_h\} [\![u_h]\!] \, \mathrm{d}s \end{aligned} \tag{3.43}$$

$$J(u_h, v_h) = \eta \int_{\Gamma_{int}} \frac{\hat{\sigma}_\gamma}{h_\gamma} [\![u_h]\!] [\![v_h]\!] \, \mathrm{d}s \tag{3.44}$$

$$l(v_h) = \int_{\partial\Omega} I v_h \, \mathrm{d}s. \tag{3.45}$$

The basis of the finite element space V_h is given by $\psi_1, \ldots, \psi_N$, with N being the number of unknowns. We can rewrite our discrete solution $u_h \in V_h$ as

$$u_h = \sum_{i=1}^{N} u_i \psi_i, \tag{3.46}$$

which leads, like in the CG-FEM, to the linear equation system

$$\boldsymbol{K}\boldsymbol{u} = \boldsymbol{b} \tag{3.47}$$

with the stiffness matrix $\boldsymbol{K} \in \mathbb{R}^{N \times N}$, the load vector $\boldsymbol{b} \in \mathbb{R}^N$ and the solution vector $\boldsymbol{u} \in \mathbb{R}^N$ of the DG-FEM are defined by

$$\boldsymbol{K} = (a(\psi_i, \psi_j) + J(\psi_i, \psi_j))_{1 \leq i,j \leq N} \tag{3.48}$$

$$\boldsymbol{b} = (l(\psi_i))_{1 \leq i \leq N} \tag{3.49}$$

$$\boldsymbol{u} = (u_j)_{1 \leq j \leq N}. \tag{3.50}$$

We then obtain the discrete solution u_h by solving this linear equation system with the numerical solver of choice.

4. Analytical Solution

In this chapter, we will introduce an analytical approach to solve the tES forward problem. Therefore a series expansion for the potential distribution is derived, caused by two surface electrodes in a multi-layered sphere with piecewise constant conductivities. Then we will investigate the convergence of this expansion.

4.1. Multi-layer Sphere Model

The main advantage of taking a multi-layer sphere model is that the tES forward problem in Definition 2.2 can be solved analytically. Thus, we can take the analytical solution as a reference for numerical methods.
As a validation platform, we will use a four-layer isotropic sphere model representing the compartments brain, cerebrospinal fluid (CSF), skull and skin of the human head. For the conductivities chosen we refer to [2, 13, 46]. The radii and conductivity values of the four compartments are given in Table 4.1.

Layer	Compartment	Radius in mm	Conductivities in S/m
1	Brain	78	0.33
2	CSF	80	1.79
3	Skull	86	0.01
4	Skin	92	0.43

Table 4.1.: Parametrization of the isotropic four-layer sphere model

4.2. Derivation of the Analytical Solution

For a multi-layer sphere model, the tES forward problem can be solved analytically. This was done for the case of isotropic conductivities in a three-layer sphere model in [47] and for a four-layer sphere model in [20]. In both cases, two point electrodes on the surface (one anode and one cathode) were used.
If we consider homogeneous and isotropic layers, the forward problem can be

writen as

$$\nabla \cdot (\sigma \nabla u) = \sigma(\nabla^2 u) = \sigma(\Delta u). \tag{4.1}$$

To derive the analytical solution, we start with the Laplace equation

$$\Delta u = 0. \tag{4.2}$$

In spherical coordinates (r, θ, ϕ) the Laplace equation reads [28]:

$$\Delta u = \frac{1}{r^2}\frac{\partial}{\partial r}\left(r^2 \frac{\partial u}{\partial r}\right) + \frac{1}{r^2 \sin\theta}\frac{\partial}{\partial \theta}\left(\sin\theta \frac{\partial u}{\partial \theta}\right) + \frac{1}{r^2 \sin^2\theta}\left(\frac{\partial^2 u}{\partial \phi^2}\right), \tag{4.3}$$

where r, θ and ϕ denote the range, the polar angle and the azimuthal angle. In the case of two scalp electrodes, we have azimuthal symmetry [47], which means that the potential u is independent of ϕ. This yields

$$\Delta u = \frac{1}{r^2}\frac{\partial}{\partial r}\left(r^2 \frac{\partial u}{\partial r}\right) + \frac{1}{r^2 \sin\theta}\frac{\partial}{\partial \theta}\left(\sin\theta \frac{\partial u}{\partial \theta}\right) = 0. \tag{4.4}$$

We use the method of separation of variables $u(r, \theta) = R(r)\Theta(\theta)$. We substitute this in equation (4.4) and multiply by $r^2/R\Theta$:

$$\underbrace{\frac{1}{R}\frac{\partial}{\partial r}\left(r^2 \frac{\partial R}{\partial r}\right)}_{\text{function of } r} = \underbrace{-\frac{1}{\Theta \sin\theta}\frac{\partial}{\partial \theta}\left(\sin\theta \frac{\partial \Theta}{\partial \theta}\right)}_{\text{function of } \theta}. \tag{4.5}$$

Because equation (4.5) has two terms of different variables, we can separate it into two ordinary differential equations. Each side is constant and the sum of those constants is zero. We choose the constant $C = l(l+1)$ and get the ordinary differential equation system:

$$\frac{1}{R}\frac{\partial}{\partial r}\left(r^2 \frac{\partial R}{\partial r}\right) = l(l+1) \tag{4.6}$$

$$\frac{1}{\Theta \sin\theta}\frac{\partial}{\partial \theta}\left(\sin\theta \frac{\partial \Theta}{\partial \theta}\right) = -\, l(l+1). \tag{4.7}$$

Solutions of the radial equation (4.6) are powers of r: By substituting $R(r) = r^s$, it follows that

$$\frac{\partial}{\partial r}\left(r^2 \frac{\partial r^s}{\partial r}\right) = \frac{\partial}{\partial r}(r^2 s r^{s-1}) = s(s+1)r^s = l(l+1)r^s. \tag{4.8}$$

Then $R(r)$ has two solutions

$$R(r) = r^l \text{ and } R(r) = \frac{1}{r^{l+1}}. \tag{4.9}$$

Therefore a general solution of the radial equation (4.6) is

$$R(r) = Ar^l + Br^{-(l+1)}. \tag{4.10}$$

The angular equation (4.7) is the Legendre equation. The solutions of the Legendre equation are Legendre polynomials $P_l(\cos\theta)$ [29].
So, the general solution of the Laplace equation in spherical coordinates with azimuthal symmetry is

$$u(r,\theta) = \sum_{k=0}^{\infty} \left(A_k r^k + B_k r^{-(k+1)}\right) P_k(\cos\theta), \tag{4.11}$$

where P_k is the Legendre polynomial of order k. To generate the solution for two surface electrodes, coordinate rotation and linear superposition are used. In a four-layer sphere model, we get the solution

$$u^{(\alpha)}(r,\theta) = \sum_{k=0}^{\infty} \left(A_k^{(\alpha)} r^k + B_k^{(\alpha)} r^{-(k+1)}\right) \left[P_k(\cos\theta_{\mathcal{A}}) - P_k(\cos\theta_{\mathcal{B}})\right], \tag{4.12}$$

where $\mathcal{A}$ and $\mathcal{B}$ denote the anode and cathode position. The expansion coefficients $A_n^{(\alpha)}$ and $B_n^{(\alpha)}$ can be determined by the boundary conditions for each tissue α. We used the expansion constants $A_n^{(\alpha)}$ and $B_n^{(\alpha)}$ given in [20].

4.3. Convergence of the Analytical Solution

In this section, we will investigate the convergence of the analytical solution by solving the forward problem in a multi-layer sphere model. The parameters chosen for the sphere model are given in Table 4.1.
When numerically computing the series expansion of the analytical solution, the infinite sum in (4.12) must be approximated by a finite sum with n terms. In Figure 4.2 we visualized the potential on the surface of the sphere and the potential for a cross-section through the sphere with (a) $n = 10$, (b) $n = 20$, (c) $n = 50$ and (d) $n = 500$ expansion terms for 90° difference between the two electrodes (anode and cathode).
For the convergence analysis, we investigate how the potential converges when

we continue adding terms to the sum. In Figure 4.1 the relative error

$$RE\%(u_n, u_{1000}) = 100\frac{\|u_n - u_{1000}\|_2}{\|u_{1000}\|_2} \tag{4.13}$$

was then plotted as a function of the number of series expansion terms n for 90° difference between the surface electrodes, where u_n, u_{1000} denote the analytical solution vector, solved on a $1mm$ grid. Also the convergence of the analytical potential solution for randomly distributed electrode positions on the surface was investigated. The convergence rates were similar as the one presented in Figure 4.1.
In further analysis, the number of iterations used in the series expansion is fixed to $n = 200$ for the analytical solution of tES.

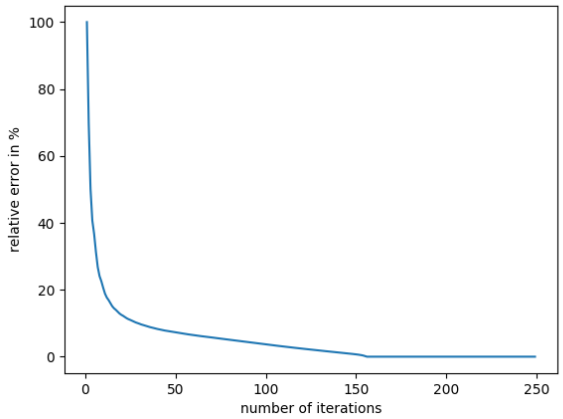

Figure 4.1.: The relative error of the analytical solution is plotted against the number of iterations used in the series expansion.

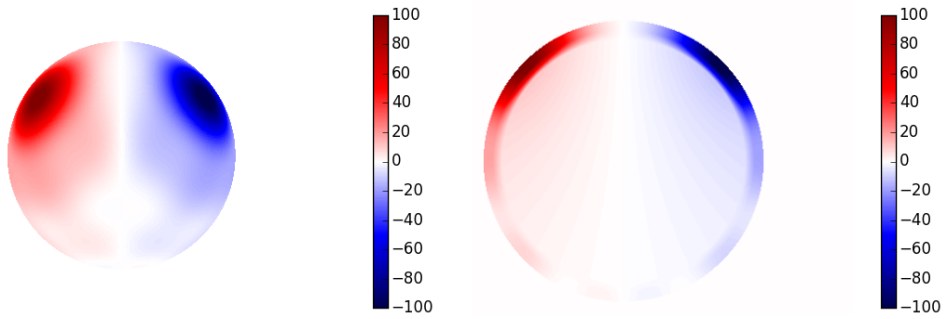

(a) Analytical solution for $n = 10$

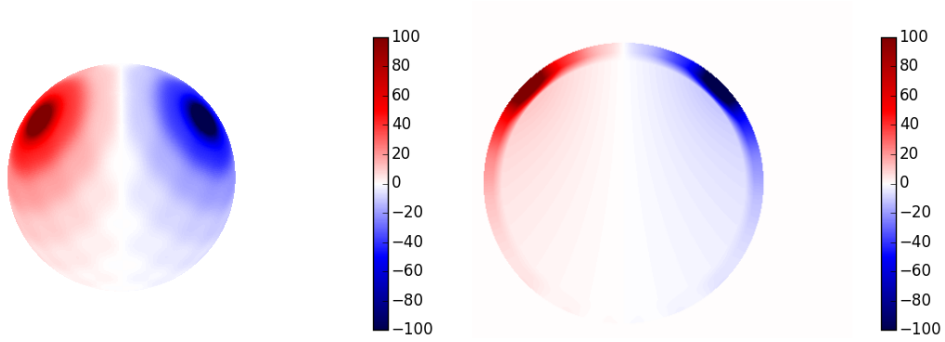

(b) Analytical solution for $n = 20$

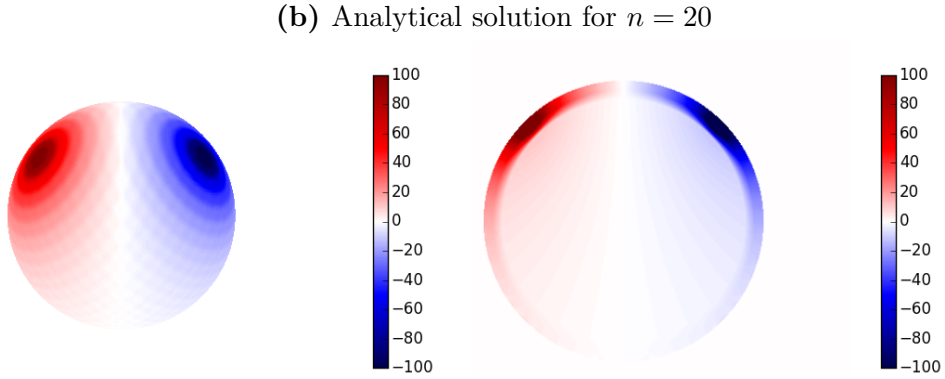

(c) Analytical solution for $n = 50$

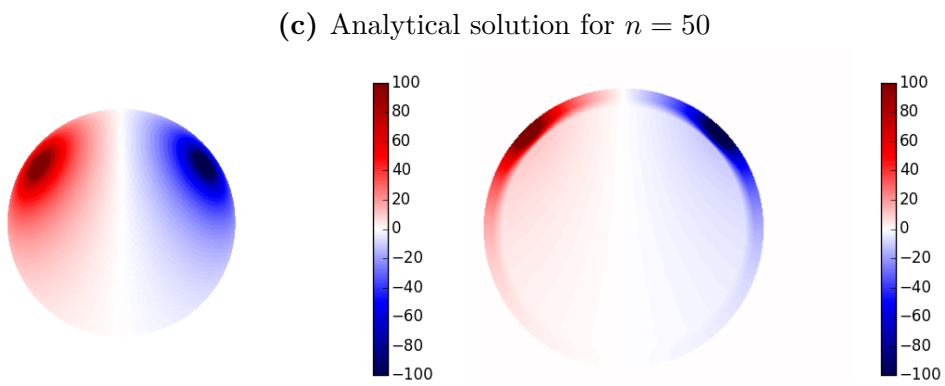

(d) Analytical solution for $n = 200$

Figure 4.2.: Different number of expansion terms for the approximation of the potential distribution on the surface of the sphere (left column) and in a cross-section through the sphere (right column).

5. Numerical Evaluation

In this chapter, we will compare the finite element methods (CG-FEM and DG-FEM) from Chapter 3 for transcranial electric stimulation. The finite element methods are implemented in *duneuro*. For the computation of the forward solutions *duneuro-python* is used. We use a spherical representation of the head in our studies to evaluate the accuracy of the finite element methods since in sphere models an analytical solution exists (Section 4.2). For the evaluation, we first use tetrahedral and than hexahedral meshes.
In the first study (Section 5.2), we will investigate tetrahedral meshes generated using a constrained Delauney triangulation (CDT) [49]. The advantage of triangular meshes is, that they fit better to the rather smooth surfaces of human tissue than the staircase-like representation in hexahedral meshes. The construction of tetrahedral meshes with CDT needs non-intersecting surfaces with a certain distance between each other, to fulfill the quality and volume constraints. Hence, the generation tetrahedral meshes requires a higher effort.
In the second study (Section 5.3), we will investigate hexahedral models. Hexahedral models have the advantage that they can be easily obtained from the voxel-based magnetic resonance imaging (MRI), where the voxels are used as elements of the mesh. Therefore less preliminary work has to be done.
The drawback of hexahedral meshes is that due to the staircase-like representation of the boundaries, in parts where the skull compartment is very thin in reality separated compartments (skin and CSF or brain) touch and cause current leakages [50]. Because of the isolating property of the low-conductive skull compartment, this then leads to an unrealistic modeling of the potential. In Study 3 (Section 5.4) we will therefore investigate hexahedral models with current leakages.
Section 5.5 shows the current density differences for the numerical approaches in the hexahedral models with skull leakages.
For all models, we use the same electrode positions. We fix them over the leakages of the hexahedral models and use this configuration in all sphere studies. The chapter ends in Section 5.6 with a conclusion.

5.1. Error Measures

To validate EEG and MEG forward approaches in sphere models the relative difference measure (RDM) and the logarithmic magnitude error (lnMAG) at the sensors are commonly used. This is no option for tES because the current is injected at the electrodes. We are interested in local changes, so the solutions are evaluated in the whole volume conductor. Therefore, the global relative error ($RE\%$) and the local relative error in each element are used as validation criteria to compare the analytical and the numerical solution of tES in sphere models. The global relative error ($RE\%$) is defined by

$$RE\%(u_{num}, u_{ana}) = 100 \frac{\|u_{num} - u_{ana}\|_2}{\|u_{ana}\|_2}, \tag{5.1}$$

where u_{num} is the numerical and u_{ana} is the analytical solution vector. Because we want to evaluate local changes of the potential, we take as the main error measure the local relative error

$$Err\%(u_{num}(c), u_{ana}(c)) = 100 \frac{|u_{num}(c) - u_{ana}(c)|}{|u_{ana}(c)|} \tag{5.2}$$

for each element centroid c and visualize this error in each corresponding element. Also the local absolute error

$$AErr\%(u_{num}(c), u_{ana}(c)) = |u_{num}(c) - u_{ana}(c)| \tag{5.3}$$

for each element is evaluated.

5.2. Study 1: Tetrahedral Models

In this study, we will evaluate the continuous Galerkin method for solving the tES forward problem presented in Section 3.1. Therefore, we investigate the potential for two fixed electrodes on the surface. We compare the results in two four-layer tetrahedral meshes depicted in Table 5.1 and visualized in Figure 5.1. To create these sphere models, a constrained Delaunay-triangulation [49] is used. The two used tetrahedral sphere models mainly differ in mesh resolution.

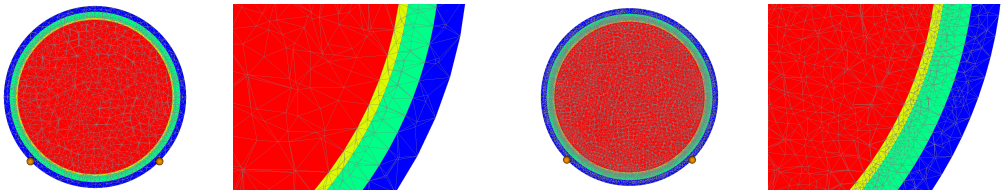

(a) tet-4layer-60k **(b)** tet-4layer-434k

Figure 5.1.: Visualization of the tetrahedral sphere models **(a)** tet-4layer-60k and **(b)** tet-4layer-434k.

model	# nodes	# elements
tet-4layer-60k	60,407	345,262
tet-4layer-434k	434,521	2,555,564

Table 5.1.: Parameter of the tetrahedral sphere models.

The models are analyzed via the global relative error $RE\%$ (5.1), the local relative error $Err\%$ (5.2) and the absolute error $AErr\%$ (5.3) in each element. These results of numerical accuracies are visualized in cross-sections through the sphere.

To demonstrate the accuracy of the numerical finite element solutions in conforming tetrahedral models, the visualizations in Figures 5.2 and 5.3 are generated.

Figure 5.2 shows cross-sections of the tet-4layer-60k model cut through the plane where the electrodes are located. In **(a)** the simulated potential distribution for the CG-FEM is shown. **(b)** shows the potential restricted to the brain compartment. In **(c)** and **(d)** the local relative and the local absolute error in the brain compartment are visualized.

Figure 5.3 shows an identically structured plot for the tet-4layer-434k model.

In Table 5.2, the global relative error is listed for both tetrahedral models in the whole volume conductor, restricted to the brain and restricted to the CSF compartment.

model	$RE\%$	$RE\%$ (brain)	$RE\%$ (CSF)
tet-4layer-60k	2.4260 %	0.5949 %	0.5145 %
tet-4layer-434k	1.2874 %	0.1441 %	0.1248 %

Table 5.2.: The global relative error for tetrahedral models.

First of all, the high relative error in **(c)** in the middle of both volume conductors is due to the fact that the local relative error is used. Because the

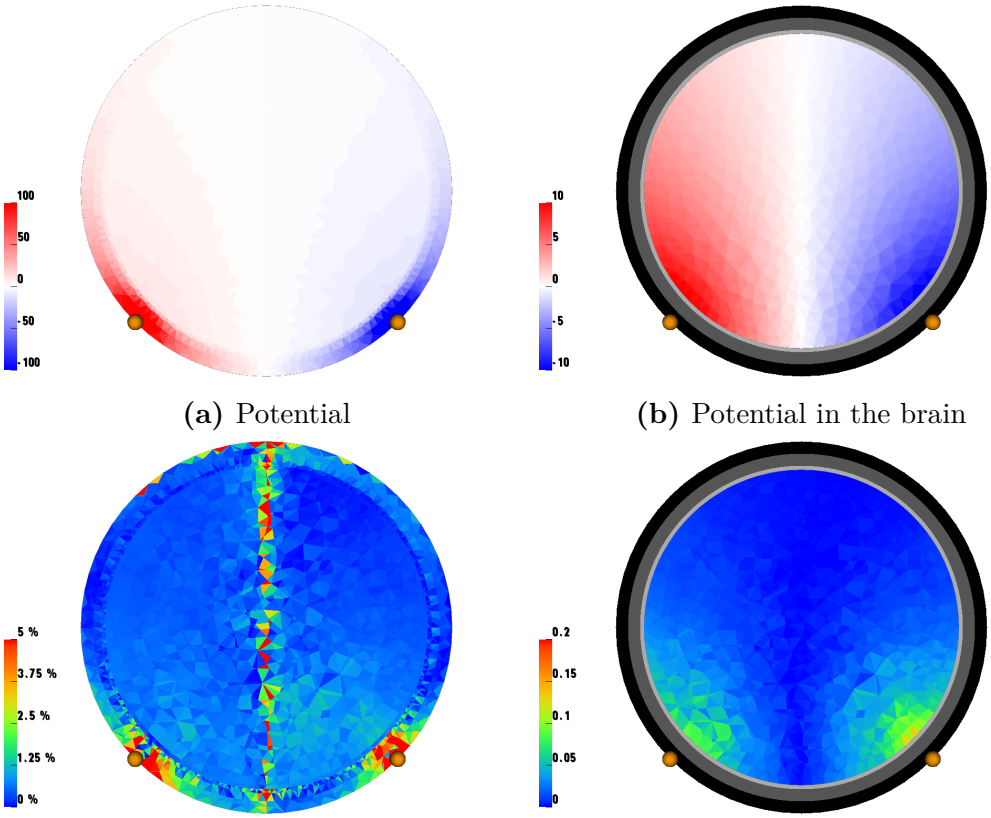

(a) Potential **(b)** Potential in the brain

(c) Relative error **(d)** Absolute error in the brain

Figure 5.2.: The numerical solution in the tet-4layer-60k sphere model for tES forward problem **(a)** in the whole volume conductor and **(b)** just the brain compartment. Visualization of the **(c)** relative error and **(d)** the absolute error between numerical and analytical solution in the brain compartment.

analytical solution is zero in the middle of the volume conductor, the relative error explodes here. For clarifying the aforementioned statement, also the absolute error **(d)** is visualized, where is seen that the difference between numerical and analytical solution is very small in this area.
Apart from that, it is observed that in the two models the highest absolute errors in the brain are under the electrodes, because here the analytical and numerical solutions of the potential are highest.
If the CG-FEM is used in the coarser mesh tet-4layer-60k, high relative errors mainly occur in the skin. Under the electrodes is the relative error also high in the skull, while in the CSF the error gets smaller. This corresponds to the results in Table 5.2, where can be seen that the global error is much higher in the whole volume conductor ($RE\% : 2.43\%$) compared to the brain ($RE\% : 0.59\%$) and CSF ($RE\% : 0.51\%$) compartments. This can be explained by the relative

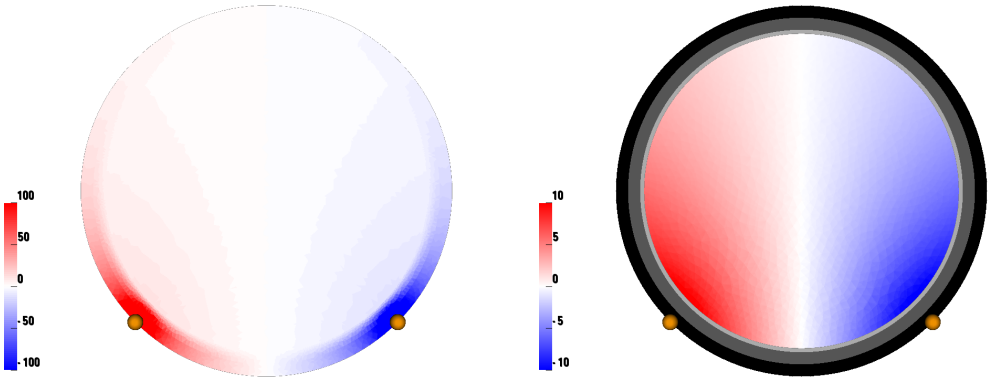

(a) Potential **(b)** Potential in the brain

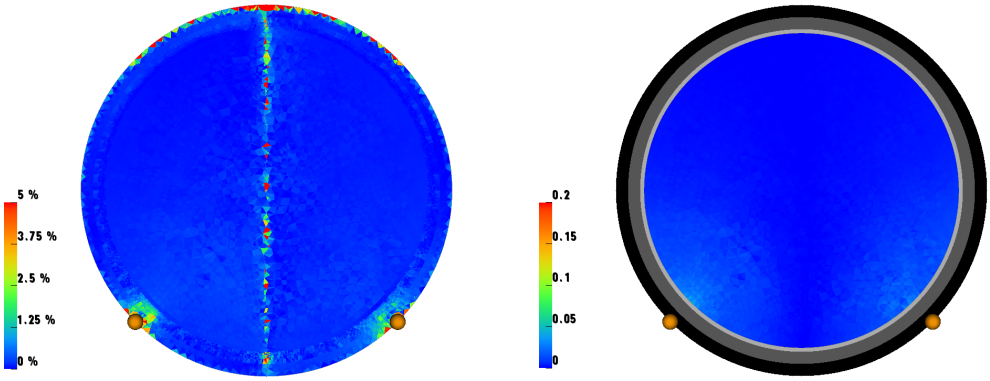

(c) Relative error **(d)** Absolute error in the brain

Figure 5.3.: The numerical solution in the tet-4layer-434k sphere model for tES forward problem **(a)** in the whole volume conductor and **(b)** just the brain compartment. Visualization of the **(c)** relative error and **(d)** the absolute error between numerical and analytical solution in the brain compartment.

coarse representation of the skin and skull compartments in this model.
For the finer mesh tet-4layer-434k, highest errors are observed in the skin compartment near the electrodes, but these are much smaller than those in the coarser mesh. This is also shown in the results of Table 5.2, where the global error is also much higher in the whole volume conductor ($RE\% : 1.29\%$) compared to the brain ($RE\% : 0.14\%$) and CSF ($RE\% : 0.12\%$) compartments. A possible reduction of these errors might be gained by local refinement close to the electrodes or of the whole skin compartment.
If the two models are compared, in Table 5.2 can be seen that the finer mesh is almost twice as accurate in the whole volume conductor, but it is more than four times more accurate than the coarser mesh for the global relative error concerning the brain and CSF compartments.

5.3. Study 2: Hexahedral Models

In this study, we will compare and evaluate the CG-FEM method (Section 3.1) and the DG-FEM (Section 3.2) in four-layer hexahedral volume conductor models with the parameters from Table 4.1. Therefore we will again make use of the analytical solution as reference (Section 4.2).
We will here use two hexahedral sphere models. Because of the staircase-like representation of the originally smooth tissues of the sphere model, we have to distinguish between numerical and geometrical errors. Therefore we use two different models with $1mm$ and $2mm$ mesh resolution from Vorwerk [52]. Details of these two four-layer hexahedral meshes are given in Table 5.3 and they are visualized in Figure 5.4.

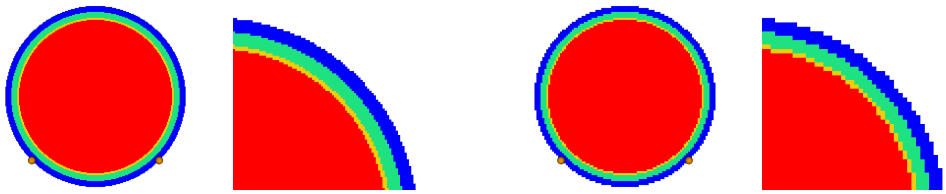

(a) hex-res-1mm **(b)** hex-res-2mm

Figure 5.4.: Visualization of the hexahedral sphere models **(a)** hex-res-1mm and **(b)** hex-res-2mm.

model	# nodes	# elements
hex-res-2mm	428,185	407,907
hex-res-1mm	3,342,701	3,262,312

Table 5.3.: Parameter of the hexahedral sphere model.

To evaluate the accuracy of the numerical approaches, the global relative error $RE\%$ and the local relative error $Err\%$ in each element are used here. We visualize the local relative error in cross-sections through the sphere.
To show the numerical results of CG-FEM and DG-FEM in hexahedral models, the visualizations shown in Figures 5.5 and 5.6 are generated.
As a first comparison between CG-FEM and DG-FEM, we visualize the potential of the numerical methods in **(a)**. Then the local relative error $Err\%$ is evaluated in the whole sphere model **(b)** and only in the brain compartment **(c)** for the model hex-res-2mm in Figure 5.5 and for the model hex-res-1mm in Figure 5.6.
The relative error $RE\%$ and the maximal local relative error in the brain and

CSF compartment for both sphere models are displayed in Table 5.4 and Table 5.5, respectively.

method	$RE\%$	max $Err\%$(brain)	max $Err\%$(CSF)
CG-FEM	7.3462 %	25.9771 %	20.7254 %
DG-FEM	6.6039 %	26.3745 %	20.1469 %

Table 5.4.: Global and maximal local relative error for the model hex-4layer-2mm.

method	$RE\%$	max $Err\%$(brain)	max $Err\%$(CSF)
CG-FEM	6.0256 %	11.7957 %	16.0424 %
DG-FEM	5.7378 %	11.4673 %	18.2624 %

Table 5.5.: Global and maximal local relative error for the model hex-4layer-1mm.

Using the hex-res-2mm sphere model with CG-FEM the visualization in Figure 5.5 shows high accuracy in the skin and skull compartments. The local relative error gets higher in the CSF and brain compartments under the electrodes. This is mainly a geometrical error for which the application of DG-FEM in those areas shows similar errors. For DG-FEM the numerical error is smaller in the whole volume conductor ($RE\% : 6.60\%$) compared to CG-FEM ($RE\% : 7.35\%$). The maximal relative error for the DG-FEM is slightly higher in the brain and slightly lower in the CSF (Table 5.4).
In Figure 5.5 the numerical methods are compared for the model hex-res-1mm. The two approaches also achieve for this model a very similar numerical accuracy. The highest numerical errors can be seen in the CSF compartment in both models.
Again the CG-FEM shows a higher global relative error ($RE\% : 6.03\%$) compared to DG-FEM ($RE\% : 5.74\%$). Interestingly other than in the $2mm$ model the maximal relative error for the DG-FEM is slightly lower in the brain and slightly higher in the CSF (Table 5.5).
Comparing the fine mesh to the coarser mesh, a clear reduction of the global relative error is seen, when increasing the mesh resolution. Even higher is the improvement if for the peak of local errors in the brain compartment. Interestingly, the improvement in the CSF compartment is not as strong.

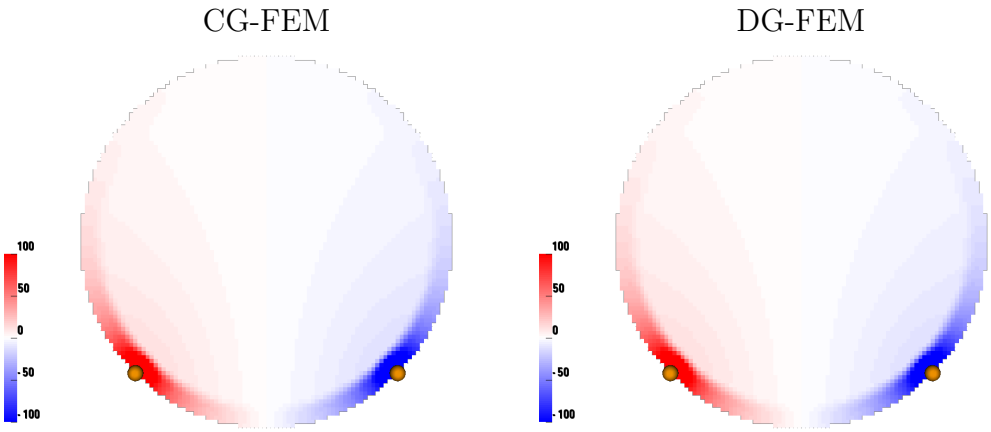

(a) Potential in the volume conductor

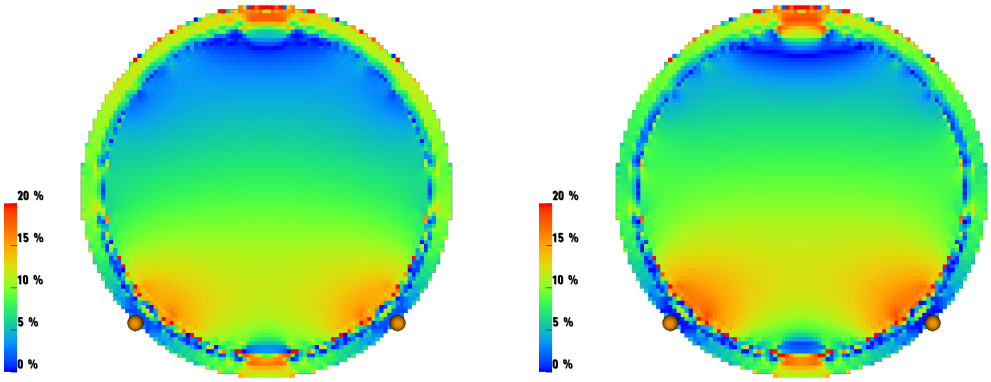

(b) Relative error

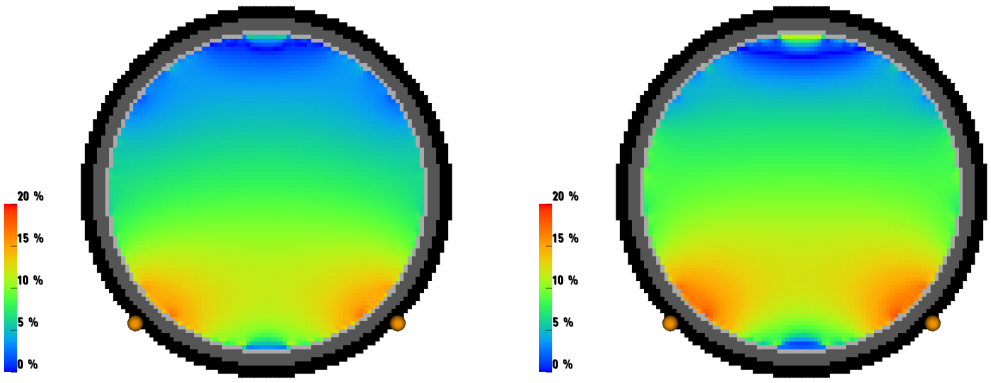

(c) Relative error in the brain

Figure 5.5.: Numerical results for hex-res-2mm sphere model CG-FEM (left) and DG-FEM (right). First, the potential solution is shown **(a)** in the sphere model. Then visualizations of the relative error **(b)** in the whole volume conductor and **(c)** only in the brain compartment are shown.

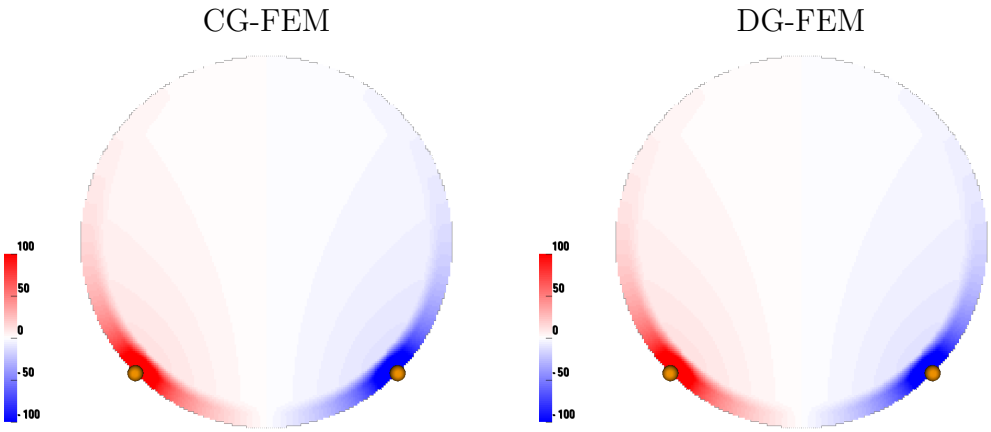

(a) Potential in the volume conductor

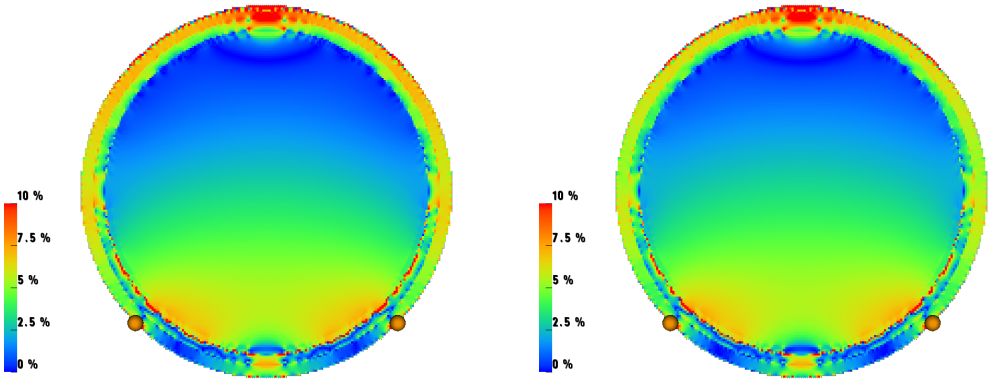

(b) Relative error

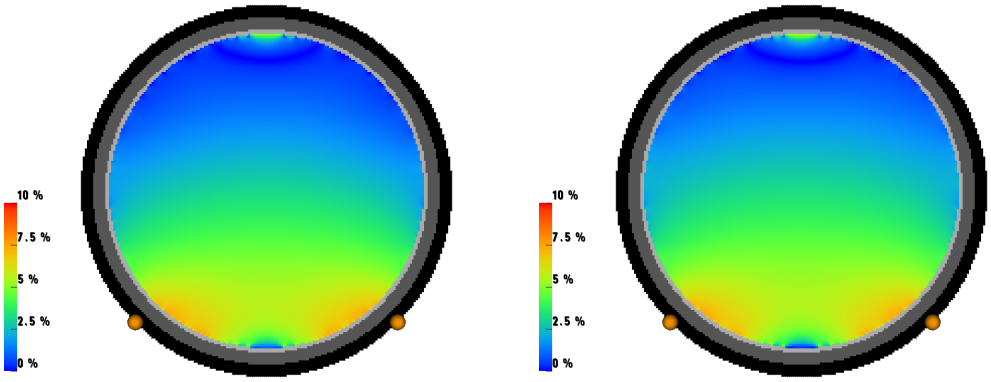

(c) Relative error in the brain

Figure 5.6.: Numerical results for hex-res-1mm sphere model CG-FEM (left) and DG-FEM (right). First, the potential solution is shown **(a)** in the sphere model. Then visualizations of the relative error **(b)** in the whole volume conductor and **(c)** only in the brain compartment are shown. Note that here the scaling of the error is different from the one in the previous figure.

5.4. Study 3: Hexahedral Models with Skull Leakages

This study is motivated by the results of Engwer and Vorwerk [17, 52], who showed for EEG that DG-FEM outperforms CG-FEM in the case of skull leakage scenarios. As discussed in the introduction of this chapter, hexahedral meshes may have the problem that in reality separated compartments are unrealistically modeled as touching at vertices. If we use the CG-FEM with Lagrange ansatz functions, this leads to unrealistic high current flow through skull leakages [17]. This effect can be reduced by using DG-FEM, where the current flows through element faces (see Figure 5.7).

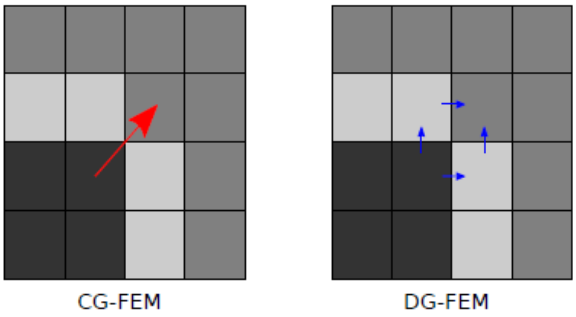

Figure 5.7.: Current flow for CG-FEM (left) and DG-FEM (right). The current flows through vertices in CG-FEM and causes current leakages. In DG-FEM current flow is only allowed through element faces. [17]

We will validate and compare the CG-FEM (Section 3.1) and the DG-FEM (Section 3.2) in four-layer hexahedral volume conductor models with leakages in the skull compartment. Thereby we will use the three models with reduced skull thickness from Vorwerk [52] with a mesh resolution of $2mm$. Details of these three four-layer hexahedral meshes are given in Table 5.6 and they are visualized in Figure 5.8. In this study, we will again use the analytical solution as reference (Section 4.2).

model	outer skull radius	leaky points
hex-res-2mm-r84	84	0
hex-res-2mm-r83	83	1,344
hex-res-2mm-r82	82	10,080

Table 5.6.: Parameter of the hexahedral sphere models with leakages.

We investigate the accuracy of the finite element methods by using the global relative error $RE\%$ and the local relative error $Err\%$ in each element. The

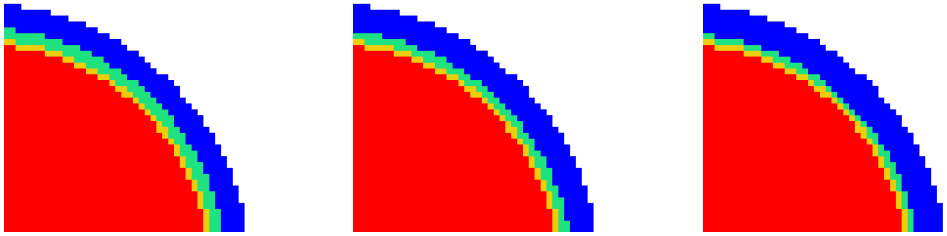

(a) hex-res-2mm-r84 **(b)** hex-res-2mm-r83 **(c)** hex-res-2mm-r82

Figure 5.8.: Visualization of the three hexahedral sphere models **(a)** hex-res-2mm-r84 **(b)** hex-res-2mm-r83 and **(c)** hex-res-2mm-r82.

local relative error is plotted in cross-sections of the sphere model. To show the influence of current skull leakages in the two numerical methods, we generated the Figures 5.9, 5.10 and 5.11.
Figure 5.9 shows cross-sections through the hex-res-2mm-r84 model. We first show the potential distribution of the numerical methods in (a). The local relative error $Err\%$ is evaluated in the whole sphere model (b) and then only in the brain compartment (c). We show an identically structured visualization of the model hex-res-2mm-r83 in Figure 5.10 and of the model hex-res-2mm-r82 in Figure 5.11. The relative error $RE\%$ and the maximal local relative error in the brain and CSF compartment of all models are shown in Table 5.7.

model	method	$RE\%$	max $Err\%$(brain)	max $Err\%$(CSF)
hex-res-2mm-r84	CG-FEM	10.2639 %	28.5111 %	23.0743 %
hex-res-2mm-r84	DG-FEM	9.2137 %	28.5902 %	22.4983 %
hex-res-2mm-r83	CG-FEM	18.9834 %	35.9705 %	42.5717 %
hex-res-2mm-r83	DG-FEM	12.0926 %	29.7925 %	26.7644 %
hex-res-2mm-r82	CG-FEM	23.9140 %	73.2800 %	79.1827 %
hex-res-2mm-r82	DG-FEM	11.8523 %	37.0218 %	40.3959 %

Table 5.7.: Global and maximal local relative error for leaky sphere models

For the model hex-res-2mm-r84, where we do not have any leakages, similar errors for CG-FEM and DG-FEM are observed. But in comparison to the hex-res-2mm model of Study 2, the error increases, which should be mainly a geometrical error.
In the other two models, higher errors in the CG-FEM compared to DG-FEM are seen, which are clearly caused by the skull leakages.
In the visualization of the local relative error for the model hex-res-2mm-r83, it is clearly shown that the leakage allows current to flow directly from the

skin compartment into the brain compartment for CG-FEM. Therefore in the brain and also in the CSF compartment, the local relative error is significantly higher for CG-FEM compared to DG-FEM. The strongest errors is found directly under the leakage.
In Table 5.7, it is shown that the global relative error $RE\%$ is 6% higher for the CG approach compared to the DG approach. The maximal local relative error $Err\%$ in the brain is 6% higher for CG-FEM and in the CSF the max. $Err\%$ is even 16% higher.
For the model hex-res-2mm-r82 with overall 10,080 leaky points, already in the potential of the volume conductor **(a)** is seen that there is almost no influence of the low-conductive skull barrier in the case of the CG approach. The current almost directly flows through the skull compartment. This unrealistic modeling is also clearly visible in the local relative error. If the two finite element approaches are compared, in CG-FEM causes the leakage an unrealistic potential in a large region under the leakage.
The CG-FEM ($RE\% : 23.91\%$) is half as accurate for the global relative error as the DG-FEM ($RE\% : 11.85\%$). If the max. relative error in the brain and CSF is investigated, the DG approach is two times more accurate (Table 5.7).

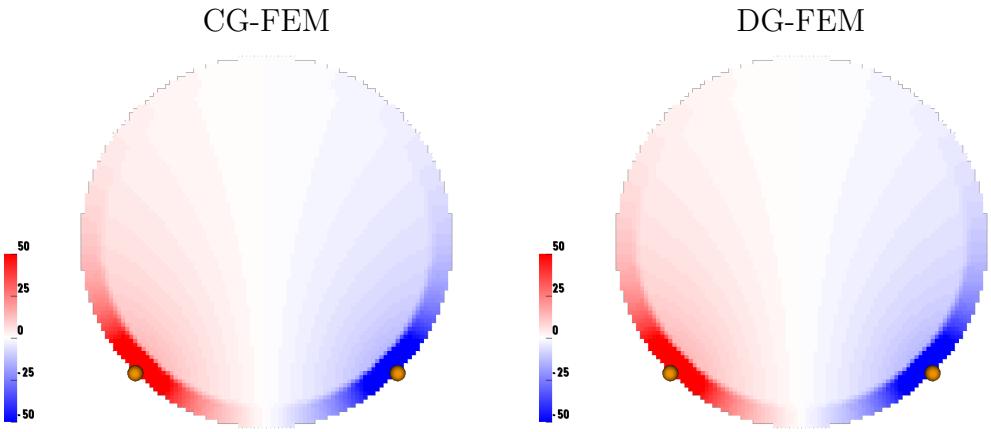

(a) Potential in the volume conductor

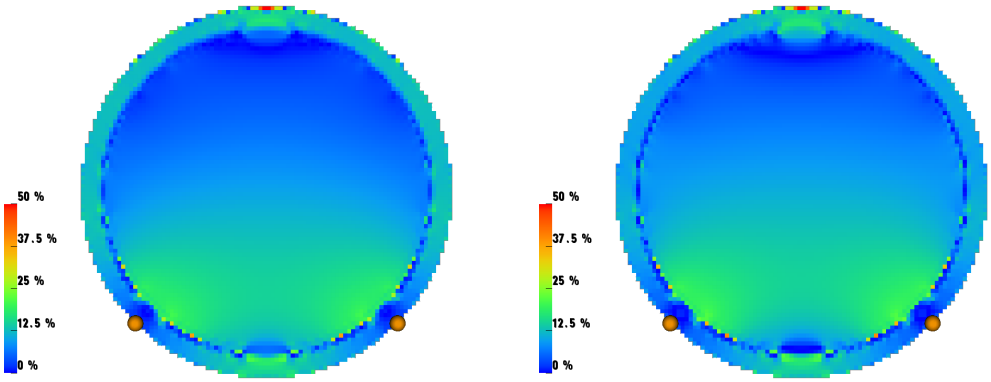

(b) Relative error

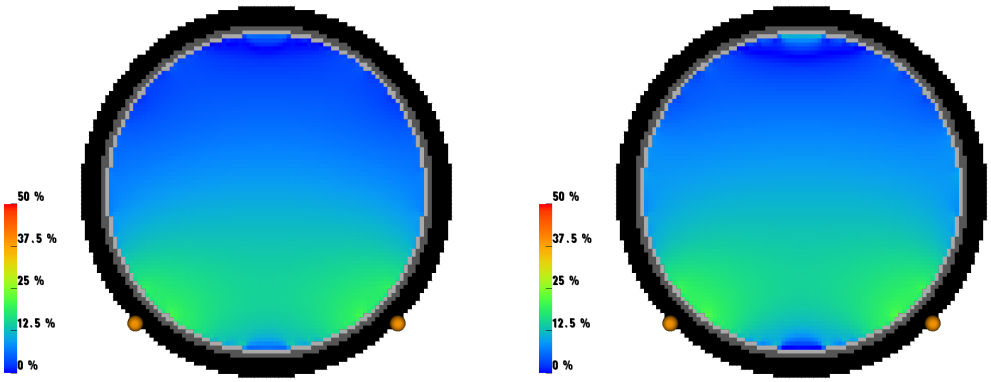

(c) Relative error in the brain

Figure 5.9.: Numerical results for hex-res-2mm-r84 sphere model CG-FEM (left) and DG-FEM (right). First, the potential solution is shown **(a)** in the sphere model. Then visualizations of the relative error **(b)** in the whole volume conductor and **(c)** only in the brain compartment are shown.

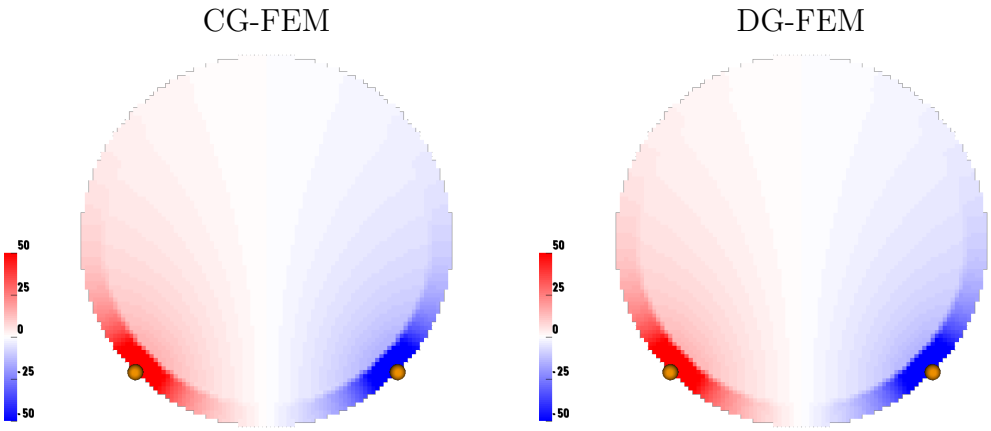

(a) Potential in the volume conductor

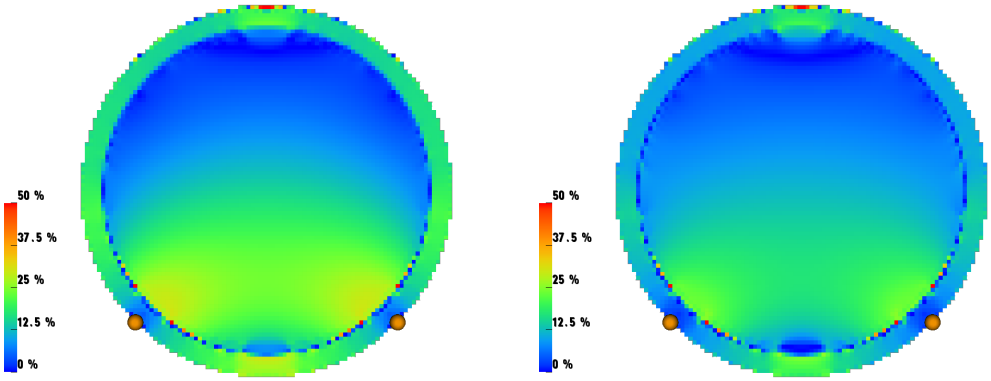

(b) Relative error

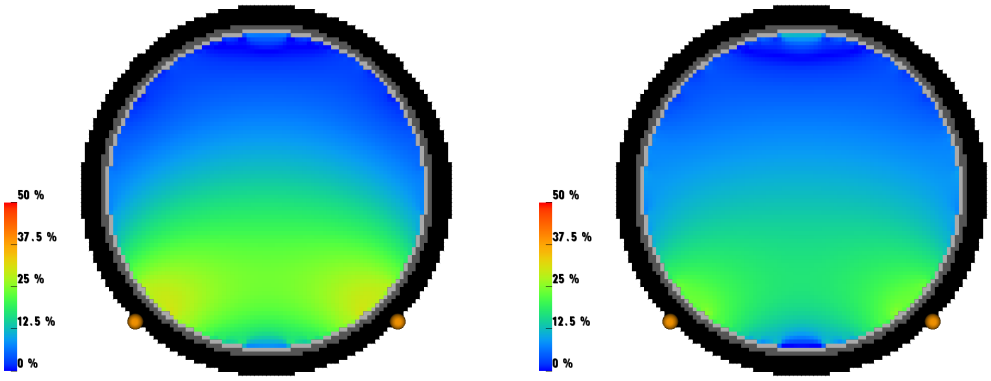

(c) Relative error in the brain

Figure 5.10.: Numerical results for hex-res-2mm-r83 sphere model CG-FEM (left) and DG-FEM (right). First, the potential solution is shown **(a)** in the sphere model. Then visualizations of the relative error **(b)** in the whole volume conductor and **(c)** only in the brain compartment are shown.

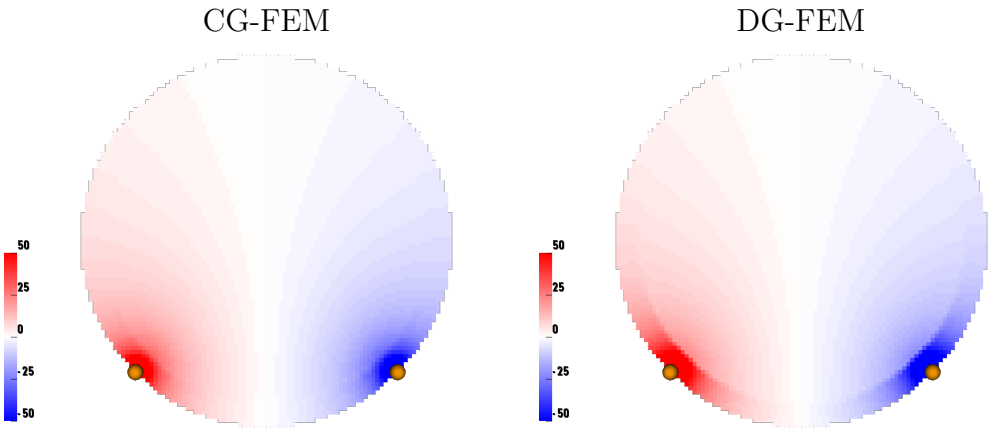

(a) Potential in the volume conductor

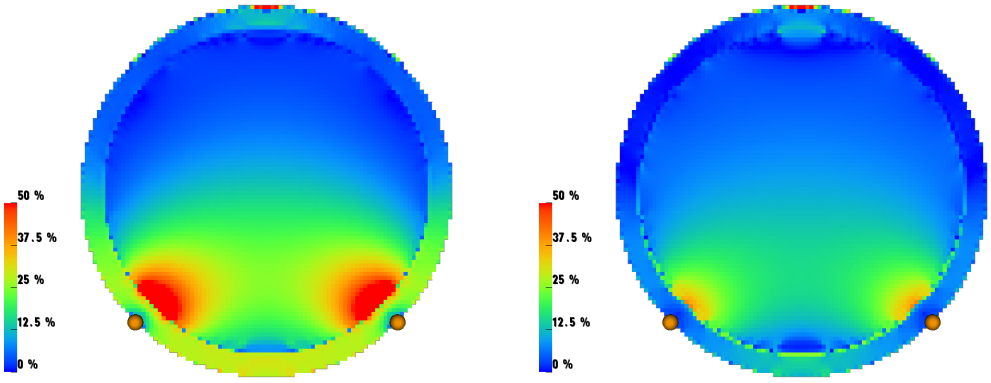

(b) Relative error

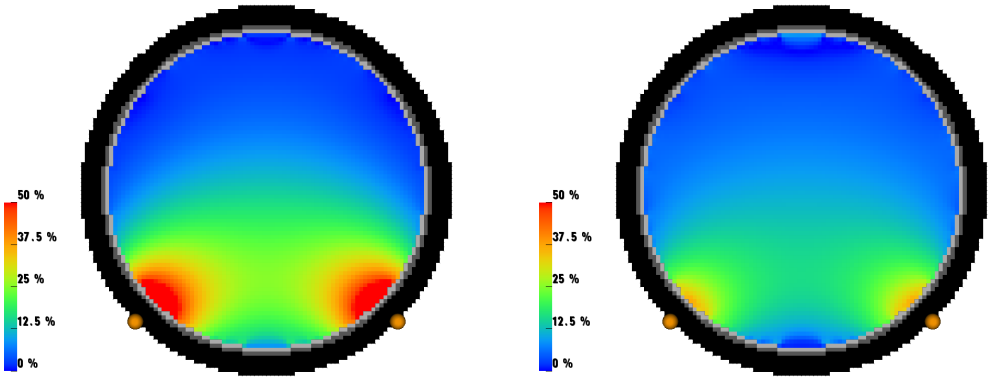

(c) Relative error in the brain

Figure 5.11.: Numerical results for hex-res-2mm-r82 sphere model CG-FEM (left) and DG-FEM (right). First, the potential solution is shown **(a)** in the sphere model. Then visualizations of the relative error **(b)** in the whole volume conductor and **(c)** only in the brain compartment are shown.

5.5. Study 4: Current Density Differences

In this section, the skull leakage effects are evaluated for the current flow in tES stimulation for CG-FEM and DG-FEM. Therefore, the current density solution $J = -\sigma \nabla u$ was computed for the same pair of electrodes as in the previous study.

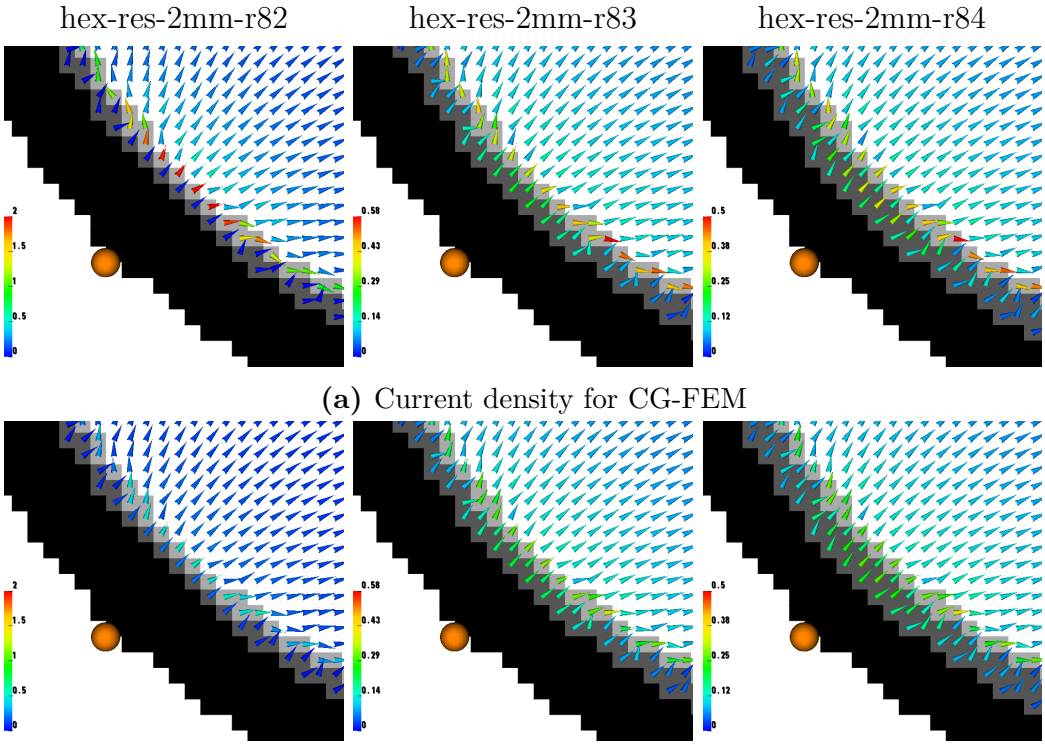

(a) Current density for CG-FEM

(b) Current-density for DG-FEM

Figure 5.12.: Visualization of current density solution for hex-res-2mm-r82 (left column), hex-res-2mm-r83 (middle column) and hex-res-2mm-r84 (right column) for **(a)** CG-FEM and **(b)** DG-FEM. Note the different scaling of the current density magnitude between models.

In Figure 5.12, the current density is visualized in the models hex-res-2mm-r82 (left column), hex-res-2mm-r83 (middle column) and hex-res-2mm-r84 (right column) for the numerical approaches CG-FEM **(a)** and DG-FEM **(b)**. For the model with the thinnest skull compartment hex-res-2mm-r82, a very high current density is found in the CSF elements directly under the electrode using the CG approach. The current density in the skull compartment is negligible, which can be explained by current leakages through the shared vertices of skin and CSF compartments. Also in the brain, the current is higher in those elements radial under the CSF elements with strong current flow. For

DG-FEM, the current in the skin is higher and in the CSF lower than for the CG approach and in the brain the current density is more realistically distributed.
For the other two models, the magnitude of the current density is much lower (note the different scaling of the current density magnitude) and the differences between CG-FEM and DG-FEM are much lower compared to the model hex-res-2mm-r82. In the models hex-res-2mm-r83 and hex-res-2mm-r84, no clear sign for skull leakages is visible, but a higher channeling of current through the highly conductive CSF compartment is seen for the CG approach. For the CSF, the elements only touch via vertices, but the geometry is connected in reality. Hence, the current is reduced for the DG approach as the current can not flow realistically through the CSF compartment. But for CG-FEM, the current flows through vertices and therefore is allowed to flow directly through this highly conductive layer.

5.6. Discussion

In this chapter, we compared CG and DG approaches to solve the tES forward problem. We presented numerical experiments in different sphere models.
In the first study, the CG-FEM was simulated in a tetrahedral sphere model. It showed high accuracy for both tetrahedral meshes.
In study 2 we investigated the differences between CG and DG approaches in two hexahedral meshes with $1mm$ and $2mm$ mesh resolution. No significant difference between the FEM approaches was found for these models. In these models, large geometrical errors were seen, due to the staircase-like representation of the geometry in hexahedral models. The first two numerical experiments showed higher numerical accuracy for tetrahedral and hexahedral meshes with increasing mesh resolution.
In the third and fourth study, the CG-FEM vs DG-FEM comparison was conducted in hexahedral models with a mesh resolution of 2mm and decreasing skull thickness to investigate the influence of skull leakages. The achieved numerical accuracy for DG-FEM were comparable to those achieved by CG-FEM in the model hex-res-2mm-r84 without leakages, while for the two models hex-res-2mm-r83 and hex-res-2mm-r82 with skull leakages the numerical accuracy was far higher for DG-FEM. Similar results were seen in [17] for the EEG forward problem.
To show the differences in the current flow we presented in Study 4 the differences in the current density between CG-FEM and DG-FEM. The skull

leakage was strongly visible in the model hex-res-2mm-r82 with most leaky vertices. In all three models, the CSF compartment was modeled too thin and therefore there are often only connections via vertices between CSF elements. These connections caused an unrealistic current flow for DG-FEM. The current was only able to flow for the CG-FEM directly through the highly conductive CSF compartment.

6. Optimization

In this chapter, we will give an introduction to the optimization problem of tES and compare the two numerical CG and DG approaches from Chapter 3 for tES optimization. The two numerical approaches are implemented in *duneuro*. The influence matrices are computed via *duneuro-python*.
We will introduce the physical background and the optimization problems mathematically. Then we will show how sensitive the optimization is to the usage of different FEM approaches in a leaky sphere model and a realistic six-compartment volume conductor head model. At last, we will conclude the results.

6.1. Basics

The inverse problem of multi-electrode tES is to optimize the electric stimulation. The goal is to determine a current injection pattern that optimally (in a certain sense) stimulates a given target or region of interest. Normally, we are interested in maximizing the current density at the target location in the target orientation while limiting the applied currents for safety reasons. The common safety criteria are the total injection current over all electrodes and the maximal current per electrode [6]. Regarding the optimization criteria, one can choose a fitting optimization procedure.
For the inverse problem, we take the results of the FEM forward problem (Chapter 3), which results in the linear equation system. To compute the electric potential, this equation system is solved. We are then able to compute the electric field $E = -\nabla\phi$ in each mesh element. And therefore we can also calculate the current density $J = \sigma E = -\sigma\nabla\phi$ in each element.

6.2. Superposition of the Current Density

In this section, we will introduce the linear superposition as the physical model of current conduction in the head. So, we will analyse the relationship between

injected currents and current density in the head. This concept was first employed for tES in [16]. If we apply currents with more than two electrodes, the stimulation is called multi-electrode tES. These $m = 1, \ldots, M$ electrodes are normally arranged like in the 10/10 or 10/20 electroencephalography (EEG) systems. The first electrode is always fixed as the reference electrode.
We compute the current density for each pair of injection electrode $m = 2, \ldots, M$ and sink (reference) electrode. So we obtain $M - 1$ independent current injection patterns.
The superposition principle now states that all other patterns can be computed from linear combinations of the following basis:

$$\boldsymbol{e} = \boldsymbol{A}\boldsymbol{s}, \tag{6.1}$$

where $\boldsymbol{A} \in \mathbb{R}^{3N \times (M-1)}$ is the tES influence matrix, $\boldsymbol{s} \in \mathbb{R}^{(M-1)}$ is the applied current vector and $\boldsymbol{e} \in \mathbb{R}^{3N}$ is the resulting current density solution. In matrix form, they are defined as follows

$$\boldsymbol{A} = \begin{pmatrix} a_1(r_1) & a_2(r_1) & \cdots & a_{M-1}(r_1) \\ a_1(r_2) & a_2(r_2) & \cdots & a_{M-1}(r_2) \\ \vdots & \vdots & \ddots & \vdots \\ a_1(r_N) & a_2(r_N) & \cdots & a_{M-1}(r_N) \end{pmatrix}, \boldsymbol{e} = \begin{pmatrix} e(r_1) \\ e(r_2) \\ \vdots \\ e(r_N) \end{pmatrix}, \boldsymbol{s} = \begin{pmatrix} s_1 \\ s_2 \\ \vdots \\ s_{M-1} \end{pmatrix}$$

where column m of $\boldsymbol{A}$ is the current density solution $J = -\sigma \nabla \phi$ for injection electrode m and sink electrode in the finite elements $r_1, \ldots, r_N$.
With this knowledge, we are now able to apply different optimization approaches. In the next section, we will introduce algorithms used to optimize applied stimulation currents.

6.3. Optimization Approaches

In tES optimization there is always a trade-off between maximizing the current in the target and the focality of the stimulation. In this section, we will mainly focus on optimization methods that will maximize the intensity.

Maximal Intensity Optimization

Following Dmochwoski [16], the maximal intensity (max int) approach is presented. In this method, we are interested in maximizing the field intensity at the target in a specific direction without considering how the current flows

elsewhere. A safety constraint is used to limit the injected currents to $2mA$. The desired orientation at the target is defined by $\boldsymbol{e_t} \in \mathbb{R}^3$. To maximize the intensity of the current flow parallel to the target orientation, the following problem is solved:

$$s_{max} = \arg\max_{s} \boldsymbol{e_t C s} \quad \text{subject to} \quad \|\tilde{\boldsymbol{s}}\| \leq 2I_{total} \tag{6.2}$$

$$\text{with } \tilde{\boldsymbol{s}} = (s_1, s_2, \cdots, s_{M-1}, -\sum s_m)^T \tag{6.3}$$

where $\tilde{\boldsymbol{s}}$ is the full current pattern including the reference electrode ($-\sum s_m$), $\boldsymbol{C} \in \mathbb{R}^{3\times M}$ is the sub-matrix of $\boldsymbol{A}$ corresponding to the target, while I_{total} is the total injected current. The linear optimization problem was solved using CVX, a package for specifying and solving convex programs [23, 24].

Penalized Maximal Intensity Optimization

Because the maximal intensity optimization always results in a bipolar electrode montage, we developed a novel stimulation approach using an additional regularization, that forces the distribution of the injection current over electrodes. We additionally limit the maximum current at each electrode to ensure safety and comfort of the stimulation in the penalized maximal intensity (penalized max int) approach. Then the following problem is solved:

$$s_{max} = \arg\max_{s} \boldsymbol{e_t C s} + \lambda\|\tilde{\boldsymbol{s}}\|_2 \quad \text{subject to} \quad \|\tilde{\boldsymbol{s}}\|_1 \leq 2I_{total} \tag{6.4}$$

$$\text{and} \quad \|\tilde{\boldsymbol{s}}\|_\infty \leq I_{max} \quad \text{with} \quad \tilde{\boldsymbol{s}} = (s_1, s_2, \cdots, s_{M-1}, -\sum s_m)^T, \tag{6.5}$$

where the regularization parameter λ forces the current distribution and I_{max} is the maximum current at each electrode. This problem was also solved using the CVX toolbox [23, 24].

tES Optimization using ADMM

The tES optimization using ADMM by Wagner et al in [54] generates a focal stimulation. This approach solves a numerical optimization problem including additional constraints of upper bounds in non- targeted areas. The constraint optimization problem to maximize the current in the target area, while con-

trolling the magnitude in other regions, is given by

$$s_{max} = \max_{s} \int_{\Omega_t} \langle \boldsymbol{As}, \boldsymbol{e} \rangle \, \mathrm{d}x \quad \text{subject to} \quad \omega |\boldsymbol{As}| \leq \epsilon, \tag{6.6}$$

where Ω_t is the target region, $\boldsymbol{e} \in \mathbb{R}^{3N}$ is the target vector, ω is a weight allowing high currents in the target region and ϵ being the upper bound in non-target regions.
To ensure convexity of the problem and control the applied currents additional L1 and L2 regularization terms were added. This leads to the regularized optimization problem:

$$\begin{aligned} s_{max} = &\max_{s} \int_{\Omega_t} \langle \boldsymbol{As}, \boldsymbol{e} \rangle \, \mathrm{d}x - \alpha \int_{\partial\Omega} \boldsymbol{s}^2 \, \mathrm{d}S + \beta \|\boldsymbol{s}\|_{L^1(\partial\Omega)} \\ &\text{subject to} \quad \omega |\boldsymbol{As}| \leq \epsilon, \end{aligned}$$

with α and β being the L1 and L2 regularization parameter. This problem was solved using the alternating direction method of multipliers (ADMM) [54], a variant of the augmented Lagrangian method.

6.4. Study 1: Optimization in a Sphere Model

In this study, we analyze the differences in the tES optimizations between CG-FEM and DG-FEM using a spherical model. The three optimization approaches introduced in Section 6.3 will be compared. The volume conductor model used here is the leaky sphere model hex-res-2mm-r82 already used in Section 5.4 with overall 10,080 leaky points. 522 point-like stimulation electrodes were distributed over the surface of the sphere model visualized in Figure 6.1. Two to the surface tangential target vectors with different target depth were used for stimulation (Figure 6.1).
The resulting stimulation and the optimized current density are shown for the three optimization approaches maximal intensity (first row), penalized maximal intensity (middle row) and optimization using ADMM (bottom row) for CG-FEM (first column) and DG-FEM (second column) in Figure 6.2 for the more superficial tangential and in Figure 6.3 for the deeper tangential target. For the superficial and for the deep target a similar behavior is seen for the current flow and for the stimulation protocols. When using CG-FEM in the max int optimization, the active electrodes are quite close to the target, resulting in a more focal current flow in the volume conductor. For DG-FEM the active electrodes are further apart. Also in the current density, a far more

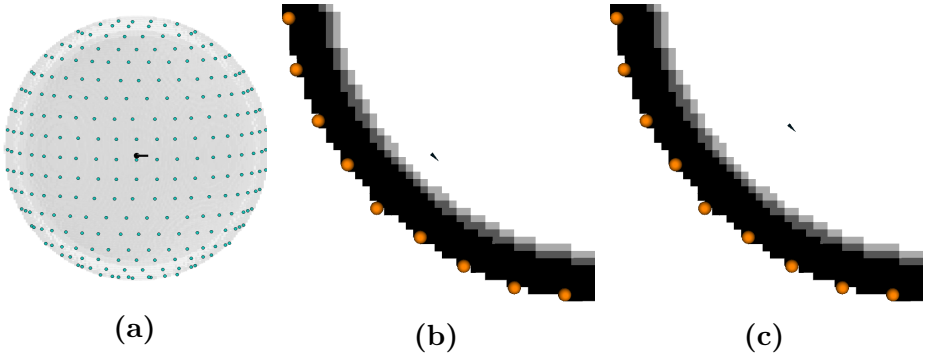

Figure 6.1.: Locations of the stimulation electrodes for the stimulation in the sphere model hex-res-2mm-r82 and of the different target vectors. The first plot **(a)** shows the electrode configuration on the sphere model. The other two plots **(b)**, **(c)** show the two target vectors in a cross-section through the volume conductor.

widespread flow is seen and therefore the current density magnitude is lower. In the penalized max int stimulation the highest currents are applied at the same electrodes as in the max int stimulation with additional active surrounding electrodes. Even if the difference between the two FEM approaches is lower than in the max int stimulation, the current flow is still more spread for DG-FEM and the magnitude of the current density is lower than for the CG approach.

For the optimization using ADMM, the two finite element methods differ least. This effect was expected, because the ADMM focuses on a focal stimulation, so the main stimulation electrodes are those close to the target. For CG-FEM the compensating currents, to reduce the applied currents in non-target regions, are higher.

The high differences for the two intesity based stimulations seem to be caused by skull leakages. In the forward problem is current flowing without much resistance from the CSF into the skin compartment (Section 5.4 and Section 5.5). Hence, an overestimation of the importance of electrodes close to the target is seen in the inverse problem for CG-FEM.

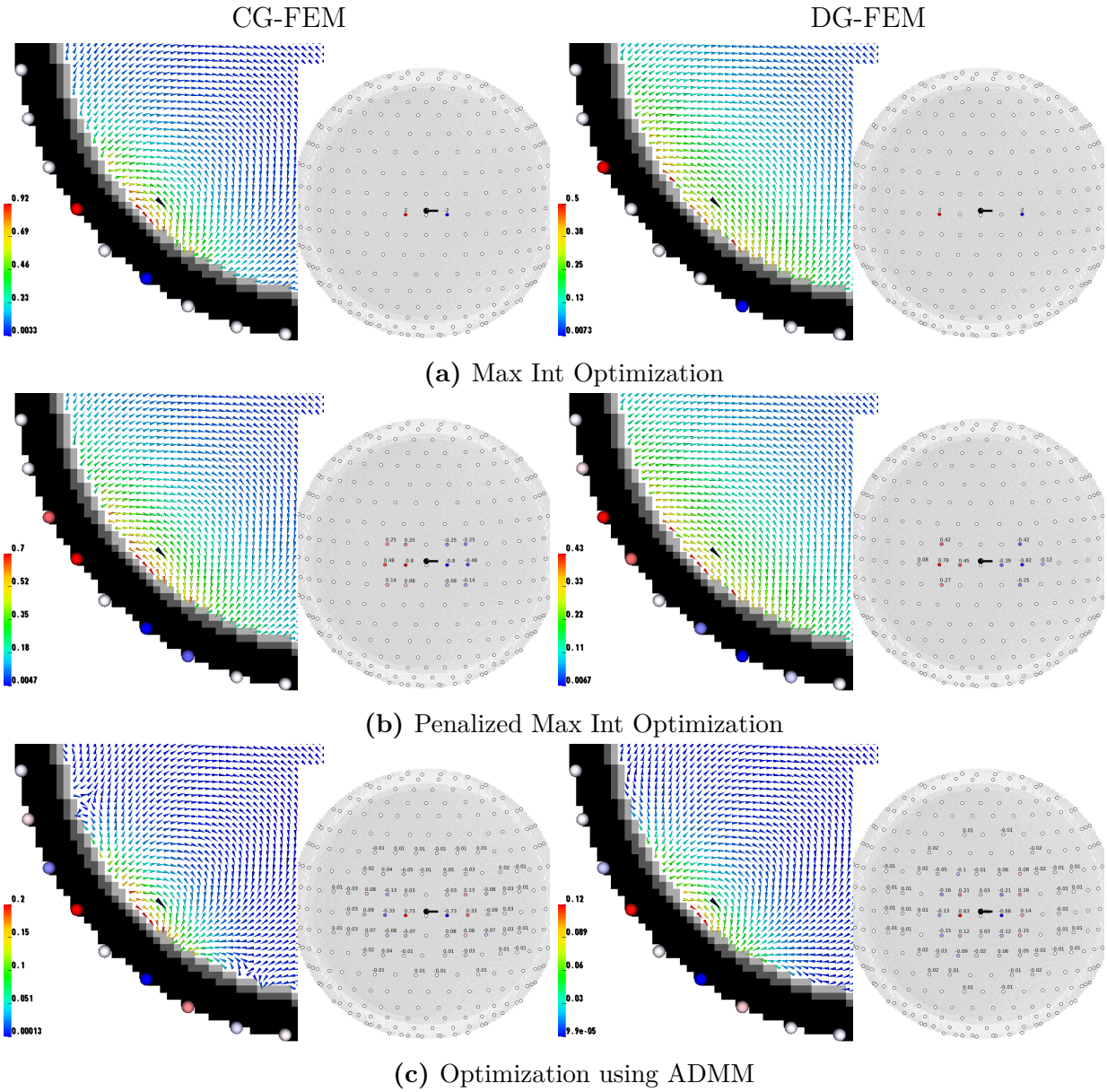

(a) Max Int Optimization

(b) Penalized Max Int Optimization

(c) Optimization using ADMM

Figure 6.2.: Visualization using **(a)** max int optimization **(b)** penalized max int optimization and **(c)** optimization using ADMM for the numerical approaches CG-FEM and DG-FEM in the leaky sphere model hex-res-2mm-r82 with a more superficial tangential target. Note that here the scaling of the current density magnitude is different in the different plots.

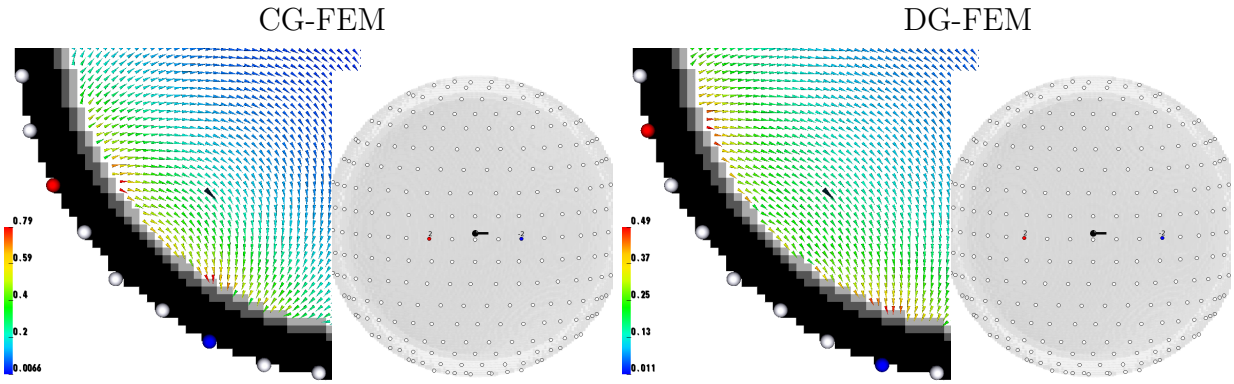

(a) Max Int Optimization

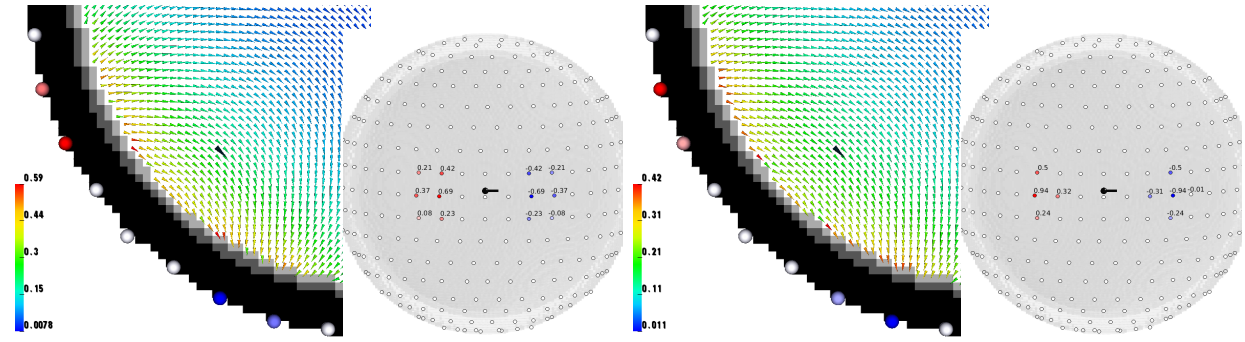

(b) Penalized Max Int Optimization

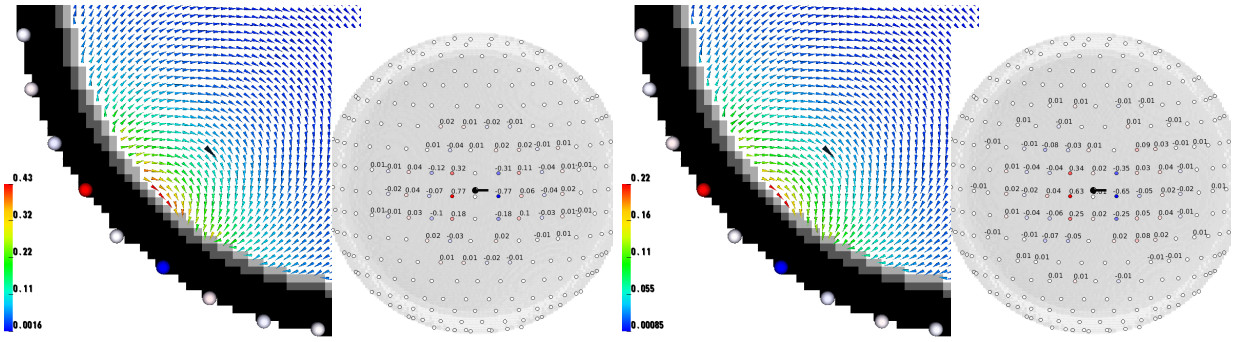

(c) Optimization using ADMM

Figure 6.3.: Visualization using **(a)** max int optimization **(b)** penalized max int optimization and **(c)** optimization using ADMM for the numerical approaches CG-FEM and DG-FEM in the leaky sphere model hex-res-2mm-r82 for the deeper tangential target. Note that here the scaling of the current density magnitude is different in the different plots.

6.5. Study 2: Optimization in a Realistic Head Model

In this study, we will validate the differences resulting from different tES optimization approaches using the two finite element methods in a realistic human head model. A six compartment segmentation including skin, skull-compacta, skull-spongiosa, CSF, gray matter and white matter is generated from T1- and T2-weighted MRI data [51]. This segmentation is used to generate a hexahedral mesh with a resolution of $2mm$ with 484,532 elements and 508,412 nodes. The model is not corrected for skull leakages. The model has 1,164 skull leakages, which are mainly located in the temporal bone. In this study, we simulate the target in the auditory cortex, because of its potential relevance in tinnitus treatment [57]. The target was located on the gray matter gyrus. The multi-channel tES cap is based on a realistic 10-10 EEG electrode configuration of 80 channels. The sensor configuration and the stimulation target are visualized in Figure 6.4.

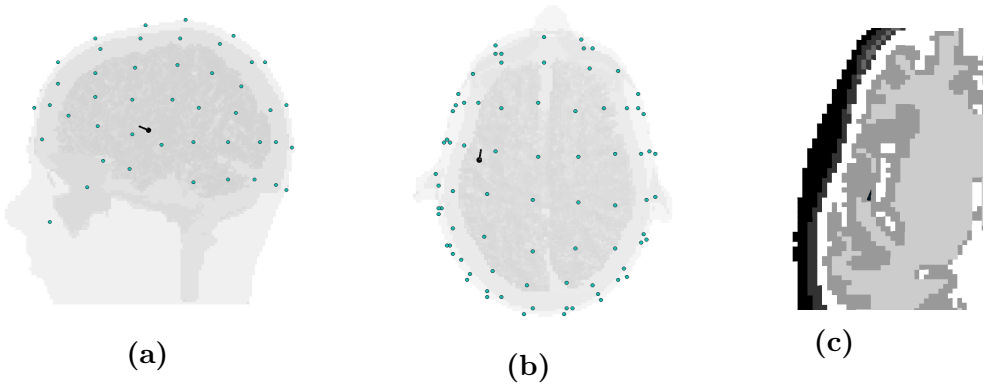

(a) **(b)** **(c)**

Figure 6.4.: Locations of the stimulation electrodes for the stimulation in the realistic head model. The first and second plot show the electrode configuration on the realistic head model from the side **(b)** and from the top **(b)**. In **(c)**, the target is shown in the axial plane of the volume conductor.

The optimal current distribution on the electrodes and the resulting current densities are displayed in Figure 6.5 for the auditory target. The three optimization approaches max int (first row), penalized max int (middle row) and optimization using ADMM (bottom row) are plotted for CG-FEM (first column) and DG-FEM (second column) in the realistic head model.
The max int stimulation results in a bipolar electrode configuration. It yields the same anode for both numerical methods but the cathodal electrode is further apart for DG-FEM.

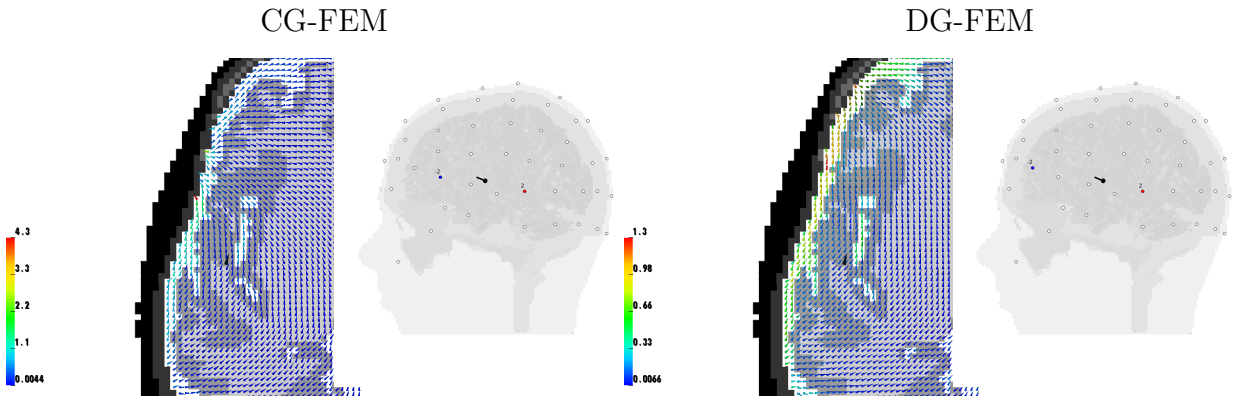

(a) Max Int Optimization

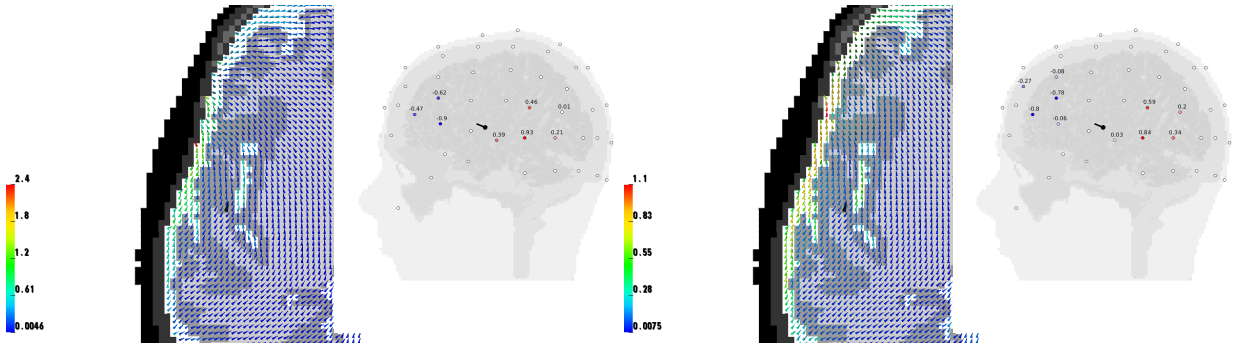

(b) Penalized Max Int Optimization

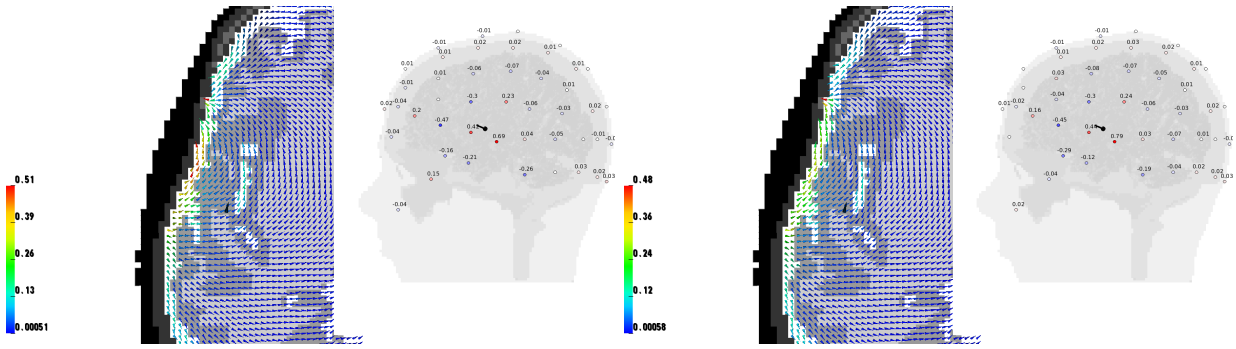

(c) Optimization using ADMM

Figure 6.5.: Visualization using **(a)** max int optimization **(b)** penalized max int optimization and **(c)** optimization using ADMM for the numerical approaches CG-FEM and DG-FEM in the realistic head model with $2mm$ resolution for an auditory target. Note that here the scaling of the current density magnitude is different in the different plots.

For the penalized max int optimization, the active electrodes are more spread. The main stimulation electrodes are those also used in the max int stimulation with additional active surrounding electrodes. The penalized max int opti-

mization differs less for the anodal stimulation between FEM approaches, but strongly differs at the cathodal electrodes. For CG-FEM the active cathodes are not as far away from the cathods as for DG-FEM. Furthermore, the stimulation electrode with the highest applied cathodal currents using CG-FEM is almost not active at all for DG-FEM.
When using ADMM optimization for archieving a focal stimulation, a broad stimulation protocol is gained. But there are only minor stimulation differences between CG-FEM and DG-FEM.
In the resultant montages, active electrodes are arranged further apart for intensity optimization using DG-FEM. This was also seen in the previous study for sphere models. The higher differences in the cathodal stimulation are explained by the location of leakages, which are mainly in the temporal bone.

6.6. Discussion

In this chapter, we presented optimization procedures for transcranial electric stimulation.
Fist, the inverse problem of tES was introduced. Following the superposition principle of current in volume conductors, we described the different tES optimization approaches as the maximal intensity approach, the penalized maximal intensity approach and the optimization approach using ADMM.
In Study 1, the differences between CG-FEM and DG-FEM for the three optimization methods in a hexahedral mesh with a $2mm$ resolution and skull leakages was investigated. The difference between the FEM approaches was not considerable for the optimization using ADMM because the ADMM focuses on a focal stimulation restricting currents in non-target areas. In the two intensity based optimization approaches, higher differences were found. The optimized stimulation electrodes were further apart for DG-FEM than for CG-FEM.
In Study 2, the optimization approaches were evaluated in a realistic shaped head model with a $2mm$ mesh resolution for CG-FEM and DG-FEM. Similar results as in the sphere study were found, but the difference was higher for the cathodal electrodes than for the anodal electrodes, because in the realistic head model the leakages were mainly located in the temporal bone.

7. Summary and Outlook

Summary

The aim of this thesis was to study finite element methods for solving the forward problem of tES and for optimizing procedures used in tES. Therefore, the continuous Galerkin (CG-FEM) and the discontinuous Galerkin (DG-FEM) approaches were presented. Both finite element methods were implemented in *duneuro* and the analytical solution in Python.
After giving the physiological background and the mathematical derivation of the tES forward problem, the existence and uniqueness of a weak solution were shown.
The CG-FEM and DG-FEM for solving the tES forward problem have been presented in Chapter 3. The DG approach was introduced in the scope of electric brain stimulation because of its higher accuracy in EEG forward simulation in leaky scenarios [17].
An analytical solution of the tES forward problem in sphere models was derived using spherical harmonics and the convergence of the analytical solution was evaluated numerically in Chapter 4.
In Chapter 5, the accuracy of CG-FEM and DG-FEM was compared in sphere models. The effect of different mesh resolutions for the tES forward solution was first investigated. Furthermore, the skull leakage effect seen for CG-FEM in EEG [17] was analyzed. In tES simulations, DG-FEM was able to prevent current leakages and model the potential and the current density more realistically.
Finally, in Chapter 6 the optimization problem of multi-electrode tES was introduced. Some background was presented and the three optimization approaches used were given. In the studies, the optimized current density fields and the optimized applied currents were visualized in a sphere model and in a realistic head model for both FEM approaches. Here, the current leakages for CG-FEM caused a more narrow stimulation protocol than in DG-FEM.

Outlook

There are several avenues along which the study of tES forward modeling and tES optimization could be advanced.
An interesting aspect that was not all evaluated in this thesis is the computational cost. The DG approaches is computationally more expensive due to the higher number of degrees of freedom and the more complex structure of the stiffness matrix. In general, the computation time of the tES optimization matrix is in the order of the transfer matrices used in the EEG inverse problem. In both modalities, a speedup could be generated by parallelizations.
Furthermore, the integration of the analytical solution into *duneuro* would be desirable. For now, the analytical solution is a Python function called via the Python script. A further modality that could be implemented in *duneuro* is the transcranial magnetic stimulation (TMS).
Geometrical errors could be reduced by using meshes that best fit the underlying geometry. Triangular meshes can better represent rather smooth surfaces. But then more preliminary work has to be done. To increase the accuracy geometry-adapted hexahedral meshes could be used for tES instead of regular hexahedral meshes. They will not overcome the leakage effect, but will be able to diminish the geometrical errors [56].
Promising results showed unfitted FEM approaches, like the unfitted discontinuous Galerkin FEM (UDG-FEM) and the CutFEM in EEG studies using level-set segmentations [40]. These approaches are able to reduce the geometrical errors while decreasing the computational costs.
With regard to optimization methods, an investigation of combined brain stimulation using the complementary techniques of transcranial electric and magnetic stimulation would be interesting. New optimization approaches may be needed to link the modalities.

A. Appendix

A.1. Mathematical Background

Here we will give some theory of functional analysis. We will introduce the Lebesgue space L^p and the Sobolev space W_p^k and then give some well-known theorems used in this thesis. Thereby we will mainly follow [8, 9].

Definition A.1 (Lebesgue Space $L^p(\Omega)$) Let $\Omega \subset \mathbb{R}^d$, $d \in \mathbb{N}$, be a Lebesgue-measurable non-empty open set. Then the Lebesgue norm for $1 \leq p < \infty$ of a measurable function $f : \Omega \to \mathbb{R}$ is defined by

$$\|f\|_{L^p(\Omega)} = (\int_\Omega |f(x)|^p \, \mathrm{d}x)^{1/p}. \tag{A.1}$$

Then the Lebesgue space $L^p(\Omega)$ is the set of p-integrable functions

$$L^p(\Omega) := \{f : \Omega \to \mathbb{R} | \|f\|_{L^p(\Omega)} < \infty\}. \tag{A.2}$$

Remark 1 (Hilbert Space $L^2(\Omega)$) The Lebesgue space $L^2(\Omega)$ together with the inner product

$$\langle u, v \rangle_{L^2(\Omega)} := \int_\Omega u(x)v(x) \, \mathrm{d}x \text{ for } u, v \in L^2(\Omega) \tag{A.3}$$

and norm

$$\|u\| := \sqrt{\langle u, v \rangle_{L^2(\Omega)}} \tag{A.4}$$

is a Hilbert space.

Definition A.2 (Multi-Index) A vector $\alpha \in \mathbb{R}^d, \alpha_i \in \mathbb{N}_0 \, \forall 1 \leq i \leq d$ is called a multi-index. The length of a multi-index is defined by

$$|\alpha| := \sum_{i=1}^{d} \alpha_i \tag{A.5}$$

and for $u \in C^\infty(\Omega)$ the partial derivates are defined by

$$D^\alpha u := \left(\frac{\partial}{\partial x_1}\right)^{\alpha_1} \dots \left(\frac{\partial}{\partial x_d}\right)^{\alpha_d} u. \tag{A.6}$$

Definition A.3 (Sobolev Space $W^{k,p}(\Omega)$) Let $\Omega \subset \mathbb{R}^d, d \in \mathbb{N}$ be non-empty open set and let $k \in \mathbb{N}, 1 \leq p < \infty$, then the Sobolev space is defined as

$$W^{k,p}(\Omega) := \{u \in L^p(\Omega) | D^\alpha u \in L^p(\Omega), |\alpha| \leq k\}. \tag{A.7}$$

Remark 2 (Hilbert Space $W^{k,2}(\Omega)$) The Sobolev space $H^k(\Omega) := W^{k,2}(\Omega)$ is a Hilbert space with scalar product

$$\langle u, v\rangle_{H^k(\Omega)} = \sum_{|\alpha| \leq k} \langle D^\alpha u, D^\alpha v\rangle_{L^2(\Omega)} \tag{A.8}$$

and norm

$$\|u\|_{H^k(\Omega)} = \sqrt{\langle u, u\rangle_{H^k(\Omega)}}. \tag{A.9}$$

Definition A.4 (Bounded and H-elliptic Bilinearform) Let $(H, \langle\cdot,\cdot\rangle)$ be a Hilbert space and $a : H \times H \to \mathbb{R}$ a bilinearform, then $a(\cdot,\cdot)$ is called bounded if there exists a $C \geq 0$ such that

$$|a(u, v)| \leq C\|u\|_H \|v\|_H \text{ for all } u, v \in H \tag{A.10}$$

and $a(\cdot,\cdot)$ is called H-elliptic if there exists a $c \geq 0$ such that

$$a(u, u) \geq c\|u\|_H^2 \text{ for all } u \in H. \tag{A.11}$$

Theorem A.1 *(Lax-Milgram) Let $(H, \langle\cdot,\cdot\rangle)$ be a Hilbert-space and $a(\cdot,\cdot)$ be a bounded and H-elliptic bilinearform. Then there exists for every $l(\cdot) \in H'$ a unique solution $u \in H$ of the weak formulation*

$$a(u, v) = l(v) \text{ for all } v \in H. \tag{A.12}$$

Proof. [19] □

Theorem A.2 *(Trace Theorem) Let $\Omega \subset \mathbb{R}$ be a Lipschitz domain with boundary $\partial\Omega$. Then there exists a continuous, linear map*

$$\gamma : H^1(\Omega) \to H^{1/2}(\partial\Omega) \tag{A.13}$$

with

$$\|\gamma(v)\|_{H^{1/2}(\partial\Omega)} \leq C\|v\|_{H^1(\Omega)}. \tag{A.14}$$

Proof. [8] □

A.2. Implementation of tES in *duneuro*

In this section, we will present the implementation of the tES forward problem for point-like sensors and of the optimization matrix $\boldsymbol{A}$ (Section 6.2) in *duneuro* [1] [41], a toolbox for forward modeling in neuroscience. *duneuro* is an open-source C++ software library for solving the forward problems of electroencephalography (EEG) and magnetoencephalography (MEG) and is now also able to provide simulations for electric brain stimulation. This library is built upon the Distributed and Unified Numerics Environment (DUNE) [2] [3, 4], a modular toolbox for solving partial differential equations with grid-based methods.
To make *duneuro* more conveniently usable, there exist bindings for Python [3] and Matlab [4]. This allows direct integration into established analysis pipelines. To interact with these scripting languages, an interface to the internal *duneuro* toolbox is provided. To solve the EEG and MEG forward problems the **MEEGDriverInterface** is used. For tES the provided interface class is called **TDCSPointDriverInterface**. In *duneuro* the continuous Galerkin (CG-FEM) and the discontinuous Galerkin (DG-FEM) finite element methods are implemented as fitted discretization schemes for tES. Unfitted discretization methods like the unfitted discontinuous Galerkin method and CutFEM are for now only available for EEG [41].
An example script for solving the tES forward problem and for generating the optimization matrix is presented in the following. We begin with the construction of the tDCSPointDriver.

```
import duneuropy as dp
config = {
    'type' : 'fitted',
    'solver_type' : 'cg',
    'element_type' : 'hexahedron',
    'volume_conductor' : {
        'grid.filename' : 'path_of_mesh.msh',
        'tensors.filename' : 'path_of_tensors.cond'
    },
}
```

[1] http://www.duneuro.org
[2] http://www.dune-project.org
[3] https://www.python.org
[4] https://www.mathworks.com

```
driver = dp.TDCSPointDriver3d(config)
driver.setElectrodes(electrodes, electrode_config)
```

In the driver object, the finite element method can be specified (CG-FEM or DG-FEM) in 'solver_type' and all mesh information is loaded from files given in 'volume_conductor'. After the driver is created, the electrodes can be loaded and projected onto the mesh.

```
forward_config = {
        'solver' : {
        'reduction' : 1e-9
        },
        'subtract_mean' : 'true'
}
potential=driver.solveTDCSPointForward(forward_config);
```

Next, the forward solution - the potential of the tES forward problem - is computed for a pair of two electrodes. The 'reduction' parameter indicates that the iteration of the linear solver should stop, when the relative reduction of the l_2-norm of the residuum is smaller than 10^{-9}.

```
from analytical_tES import analyticalTESsolution
analyticalSolution = analyticalTESsolution(radii,
          conductivities, anode_pos, cathode_pos,
          position, polynomials);
```

As reference, we then compute the analytical solution. The analytical solution is not yet integrated into *duneuro*. It is a Python function called via the Python script.

```
opt_config = {
        'solver' : {
        'reduction' : 1e-9
        },
}
tdcsMatrix=driver.computeTdcsMatrix(opt_config);
```

Finally, the optimization matrix is computed for a set of electrodes. The 'reduction' parameter is the same as in the forward solution. We made a direct comparison to the *duneuro*-predecessor *SimBio* [5] for the tES optimization matrix **A** with the CG-FEM - other methods are not implemented in *SimBio* - and we were able to generate the same optimization matrices for all used models.

[5] `https://www.mrt.uni-jena.de/simbio`

Bibliography

[1] Arnold, D. N., Brezzi, F., Cockburn, B., & Marini, L. D. (2002). Unified analysis of discontinuous Galerkin methods for elliptic problems. SIAM journal on numerical analysis, 39(5), 1749-1779.

[2] Baumann, S. B., Wozny, D. R., Kelly, S. K., & Meno, F. M. (1997). The electrical conductivity of human cerebrospinal fluid at body temperature. IEEE transactions on biomedical engineering, 44(3), 220-223.

[3] Bastian, P., Blatt, M., Dedner, A., Engwer, C., Klöfkorn, R., Kornhuber, R., Ohlberger, M., & Sander, O. (2008). A generic grid interface for parallel and adaptive scientific computing. part I: abstract framework. Computing, 82(2):103–119.

[4] Bastian, P., Blatt, M., Dedner, A., Engwer, C., Klöfkorn, R., Kornhuber, R., Ohlberger, M., & Sander, O. (2008). A generic grid interface for parallel and adaptive scientific computing. Part II: implementation and tests in DUNE. Computing, 82(2-3), 121-138.

[5] Bikson, M., Inoue, M., Akiyama, H., Deans, J. K., Fox, J. E., Miyakawa, H., & Jefferys, J. G. (2004). Effects of uniform extracellular DC electric fields on excitability in rat hippocampal slices in vitro. The Journal of physiology, 557(1), 175-190.

[6] Bikson, M., Grossman, P., Thomas, C., Zannou, A. L., Jiang, J., Adnan, T., ... & Brunoni, A. R. (2016). Safety of transcranial direct current stimulation: evidence based update 2016. Brain stimulation, 9(5), 641-661.

[7] Boggio, P. S., Ferrucci, R., Rigonatti, S. P., Covre, P., Nitsche, M., Pascual-Leone, A., & Fregni, F. (2006). Effects of transcranial direct current stimulation on working memory in patients with Parkinson's disease. Journal of the neurological sciences, 249(1), 31-38.

[8] Braess, D. (2007). Finite elements: Theory, fast solvers, and applications in solid mechanics. Cambridge University Press.

[9] Brenner, S., & Scott, R. (2007). The mathematical theory of finite element methods (Vol. 15). Springer Science & Business Media.

[10] Brette, R., & Destexhe, A. (Eds.). (2012). Handbook of neural activity measurement. Cambridge University Press.

[11] Brunoni, A. R., Nitsche, M. A., Bolognini, N., Bikson, M., Wagner, T., Merabet, L., ... & Ferrucci, R. (2012). Clinical research with transcranial direct current stimulation (tDCS): challenges and future directions. Brain stimulation, 5(3), 175-195.

[12] Corazza, M. F., Turovets, S., & Muravchik, C. H. (2019). Unification of optimal targeting methods in Transcranial Electrical Stimulation. bioRxiv, 557090.

[13] Dannhauer, M., Lanfer, B., Wolters, C. H., & Knösche, T. R. (2011). Modeling of the human skull in EEG source analysis. Human brain mapping, 32(9), 1383-1399.

[14] Di Pietro, D. A., Ern, A., & Guermond, J. L. (2008). Discontinuous Galerkin methods for anisotropic semidefinite diffusion with advection. SIAM Journal on Numerical Analysis, 46(2), 805-831.

[15] Di Pietro, D. A., & Ern, A. (2011). Mathematical aspects of discontinuous Galerkin methods (Vol. 69). Springer Science & Business Media.

[16] Dmochowski, J. P., Datta, A., Bikson, M., Su, Y., & Parra, L. C. (2011). Optimized multi-electrode stimulation increases focality and intensity at target. Journal of neural engineering, 8(4), 046011.

[17] Engwer, C., Vorwerk, J., Ludewig, J., & Wolters, C. H. (2017). A discontinuous Galerkin method to solve the EEG forward problem using the subtraction approach. SIAM Journal on Scientific Computing, 39(1), B138-B164.

[18] Ern, A., Stephansen, A. F., & Zunino, P. (2009). A discontinuous Galerkin method with weighted averages for advection–diffusion equations with locally small and anisotropic diffusivity. IMA Journal of Numerical Analysis, 29(2), 235-256.

[19] Evans, L. C. (2010). Partial differential equations. Second. Vol. 19. Graduate Studies in Mathematics. American Mathematical Society, Providence, RI.

[20] Ferree, T. C., Eriksen, K. J., & Tucker, D. M. (2000). Regional head tissue conductivity estimation for improved EEG analysis. IEEE Transactions on Biomedical Engineering, 47(12), 1584-1592.

[21] Ferrucci, R., Mameli, F., Guidi, I., Mrakic-Sposta, S., Vergari, M., Marceglia, S. E. E. A., ... & Priori, A. (2008). Transcranial direct current stimulation improves recognition memory in Alzheimer disease. Neurology, 71(7), 493-498.

[22] Giani, S., & Houston, P. (2011). Anisotropic hp-adaptive discontinuous Galerkin finite element methods for compressible fluid flows. International Journal of Numerical Analysis and Modeling.

[23] Grant, M. & Boyd, S. (2013). CVX: Matlab software for disciplined convex programming, version 2.0 beta. `http://cvxr.com/cvx`, September.

[24] Grant, M. & Boyd, S. (2008). Graph implementations for nonsmooth convex programs, Recent Advances in Learning and Control (a tribute to M. Vidyasagar), V. Blondel, S. Boyd, & H. Kimura, editors, pages 95-110, Lecture Notes in Control and Information Sciences, Springer. `http://stanford.edu/~boyd/graph_dcp.html`.

[25] Hackbusch, W. (2017). Elliptic differential equations: theory and numerical treatment (Vol. 18). Springer.

[26] Hallez, H., Vanrumste, B., Grech, R., Muscat, J., De Clercq, W., Vergult, A., ... & Lemahieu, I. (2007). Review on solving the forward problem in EEG source analysis. Journal of neuroengineering and rehabilitation, 4(1), 46.

[27] Hämäläinen, M., Hari, R., Ilmoniemi, R. J., Knuutila, J., & Lounasmaa, O. V. (1993). Magnetoencephalography—theory, instrumentation, and applications to noninvasive studies of the working human brain. Reviews of modern Physics, 65(2), 413.

[28] Hassani, S. (2008). Mathematical methods: for students of physics and related fields (Vol. 720). Springer Science & Business Media.

[29] Hassani, S. (2013). Mathematical physics: a modern introduction to its foundations. Springer Science & Business Media.

[30] Herculano-Houzel, S. (2009). The human brain in numbers: a linearly scaled-up primate brain. Frontiers in human neuroscience, 3, 31.

[31] Jo, J. M., Kim, Y. H., Ko, M. H., Ohn, S. H., Joen, B., & Lee, K. H. (2009). Enhancing the working memory of stroke patients using tDCS. American Journal of Physical Medicine & Rehabilitation, 88(5), 404-409.

[32] Kuo, M. F., Paulus, W., & Nitsche, M. A. (2014). Therapeutic effects of non-invasive brain stimulation with direct currents (tDCS) in neuropsychiatric diseases. Neuroimage, 85, 948-960.

[33] Lew, S., Wolters, C. H., Dierkes, T., Röer, C., & MacLeod, R. S. (2009). Accuracy and run-time comparison for different potential approaches and iterative solvers in finite element method based EEG source analysis. Applied Numerical Mathematics, 59(8), 1970-1988.

[34] Lionheart, W. R. B., Polydordes, N., Borsic, A. (2004) Chapter1: The reconstruction problem. In: Holder DS , editor. Electrical Impedance Tomography: Methods, History and Applications. London: Institute of Physics Publishing. p.3–64.

[35] Miniussi, C., Harris, J. A., & Ruzzoli, M. (2013). Modelling non-invasive brain stimulation in cognitive neuroscience. Neuroscience & Biobehavioral Reviews, 37(8), 1702-1712.

[36] Neuling, T., Wagner, S., Wolters, C. H., Zaehle, T., & Herrmann, C. S. (2012). Finite-element model predicts current density distribution for clinical applications of tDCS and tACS. Frontiers in psychiatry, 3, 83.

[37] Nitsche, M. A., & Paulus, W. (2000). Excitability changes induced in the human motor cortex by weak transcranial direct current stimulation. The Journal of physiology, 527(3), 633-639.

[38] Nitsche, M. A., Nitsche, M. S., Klein, C. C., Tergau, F., Rothwell, J. C., & Paulus, W. (2003). Level of action of cathodal DC polarisation induced inhibition of the human motor cortex. Clinical Neurophysiology, 114(4), 600-604.

[39] Nitsche, M. A., Boggio, P. S., Fregni, F., & Pascual-Leone, A. (2009). Treatment of depression with transcranial direct current stimulation (tDCS): a review. Experimental neurology, 219(1), 14-19.

[40] Nüßing, A. (2018). Fitted and Unfitted Finite Element Methods for Solving the EEG Forward Problem (Doctoral dissertation, Universität Münster).

[41] Nüßing, A., Piastra, M. C., Schrader, S., Miinalainen, T., Brinck, H., Wolters, C. H., & Engwer, C. (2019). duneuro-A software toolbox for forward modeling in neuroscience. arXiv preprint arXiv:1901.02874.

[42] Opitz, A., Paulus, W., Will, S., Antunes, A., & Thielscher, A. (2015). Determinants of the electric field during transcranial direct current stimulation. Neuroimage, 109, 140-150.

[43] Paulus, W. (2011). Transcranial electrical stimulation (tES–tDCS; tRNS, tACS) methods. Neuropsychological rehabilitation, 21(5), 602-617.

[44] Plonsey, R., & Heppner, D. B. (1967). Considerations of quasi-stationarity in electrophysiological systems. The Bulletin of mathematical biophysics, 29(4), 657-664.

[45] Rahman, A., Reato, D., Arlotti, M., Gasca, F., Datta, A., Parra, L. C., & Bikson, M. (2013). Cellular effects of acute direct current stimulation: somatic and synaptic terminal effects. The Journal of physiology, 591(10), 2563-2578.

[46] Ramon, C., Schimpf, P., Haueisen, J., Holmes, M., & Ishimaru, A. (2004). Role of soft bone, CSF and gray matter in EEG simulations. Brain topography, 16(4), 245-248.

[47] Rush, S., & Driscoll, D. A. (1969). EEG electrode sensitivity-an application of reciprocity. IEEE transactions on biomedical engineering, (1), 15-22.

[48] Sadleir, R., Vannorsdall, T. D., Schretlen, D. J., & Gordon, B. (2012). Target optimization in transcranial direct current stimulation. Frontiers in psychiatry, 3, 90.

[49] Si, H. (2015). TetGen, a Delaunay-based quality tetrahedral mesh generator. ACM Transactions on Mathematical Software (TOMS), 41(2), 11.

[50] Sonntag, H., Vorwerk, J., Wolters, C. H., Grasedyck, L., Haueisen, J., & Maeß, B. (2013, September). Leakage effect in hexagonal FEM meshes of the EEG forward problem. In International Conference on Basic and Clinical Multimodal Imaging (BaCI) (Vol. 102).

[51] Vorwerk, J., Cho, J. H., Rampp, S., Hamer, H., Knösche, T. R., & Wolters, C. H. (2014). A guideline for head volume conductor modeling in EEG and MEG. NeuroImage, 100, 590-607.

[52] Vorwerk, J. (2016). New finite element methods to solve the EEG/MEG forward problem (Doctoral dissertation, Westfälische Wilhelms-Universität Münster).

[53] Wagner, S., Rampersad, S. M., Aydin, Ü., Vorwerk, J., Oostendorp, T. F., Neuling, T., ... & Wolters, C. H. (2013). Investigation of tDCS volume conduction effects in a highly realistic head model. Journal of neural engineering, 11(1), 016002.

[54] Wagner, S., Burger, M., & Wolters, C. H. (2016). An optimization approach for well-targeted transcranial direct current stimulation. SIAM Journal on Applied Mathematics, 76(6), 2154-2174.

[55] Wolters, C. H., Köstler, H., Möller, C., Härdtlein, J., Grasedyck, L., & Hackbusch, W. (2007). Numerical mathematics of the subtraction method for the modeling of a current dipole in EEG source reconstruction using finite element head models. SIAM Journal on Scientific Computing, 30(1), 24-45.

[56] Wolters, C. H., Anwander, A., Berti, G., & Hartmann, U. (2007). Geometry-adapted hexahedral meshes improve accuracy of finite-element-method-based EEG source analysis. IEEE Transactions on Biomedical Engineering, 54(8), 1446-1453.

[57] Zaehle, T., Beretta, M., Jäncke, L., Herrmann, C. S., & Sandmann, P. (2011). Excitability changes induced in the human auditory cortex by transcranial direct current stimulation: direct electrophysiological evidence. Experimental brain research, 215(2), 135.